







Novel Atmospherically Plasma Sprayed Micro Porous Layer for Anion Exchange Membrane Water Electrolysis Operating With Supporting Electrolyte

'incent Wilke ^{l 📵} Marco Rivera ^l Tobias Morawietz ^l Noriko Sata ^l Lukas Mues ² Manuel Hegelheimer ³	
rtjom Maljusch ⁴ Patrick Borowski ⁴ Günter Schmid ⁵ Chen Yie Thum ⁶ Malte Klingenhof ⁶ Peter Strasser ⁶	5
ındré Karl ⁷ 📵 Shibabrata Basak ⁷ Jean-Pierre Poc ^{7,8} 📵 Rüdiger-A. Eichel ^{7,8} Aldo Saul Gago ¹ 📵	
aspar Andreas Friedrich ¹	

¹Institute of Engineering Thermodynamics, German Aerospace Center (DLR), Stuttgart, Germany | ²Institute of Engineering Thermodynamics, German Aerospace Center (DLR), Oldenburg, Germany | ³Helmholtz-Institute Erlangen-Nürnberg for Renewable Energy (IET-2), Forschungszentrum Jülich GmbH (FZJ), Erlangen, Germany | ⁴Evonik Operations GmbH, Paul-Baumann-Straße 1, Marl, Germany | ⁵Siemens Energy Global GmbH & Co. KG, Erlangen, Germany | ⁶Department of Chemistry, Chemical Engineering Division, Technical University Berlin (TUB), Berlin, Germany | ⁷Institute of Energy Technologies, Fundamental Electrochemistry (IET-1), Forschungszentrum Jülich GmbH, Jülich, Germany | ⁸Institute of Physical Chemistry, RWTH Aachen University, Aachen, Germany

Correspondence: Aldo Saul Gago (aldo.gago@dlr.de)

Received: 30 September 2024 | Revised: 23 November 2024 | Accepted: 25 November 2024

Funding: This research was supported by the project AEM-Direkt (Förderkennzeichen 03HY130) funded by the German Ministry of Science and Education (BMBF).

Keywords: anion exchange membrane water electrolysis (AEMWE) | atmospheric plasma spraying (APS) | micro porous layer (MPL)

ABSTRACT

Anion exchange membrane water electrolysis (AEMWE) is one of the most promising candidates for green hydrogen production needed for the de-fossilization of the global economy. As AEMWE can operate at high efficiency without expensive Platinum Group Metal (PGM) catalysts or titanium cell components, required in state-of-the-art proton exchange membrane electrolysis (PEMWE), AEMWE has the potential to become a cheaper alternative in large-scale production of green hydrogen. In AEMWE, the porous transport layer and/or micro porous layer (PTL/MPL) has to balance several important tasks. It is responsible for managing transport of electrolyte and/or liquid water to the catalyst layers (CLs), transport of evolving gas bubbles away from the CLs and establishing thermal and electrical connection between the CLs and bipolar plates (BPPs). Furthermore, especially in case the CL is directly deposited onto the MPL, forming a catalyst-coated substrate (CCS), the MPL surface properties significantly impact CL stability. Thus, the MPL is one of the key performance-defining components in AEMWE. In this study, we employed the flexible and easily upscaled technique of atmospheric plasma spraying (APS) to deposit spherical nickel coated graphite directly on a low-cost mesh PTL. Followed by oxidative carbon removal, a nickel-based MPL with superior structural parameters compared to a state-of-art nickel felt MPL was produced. Due to a higher activity of the nickel APS-MPL itself, as well as improved catalyst utilization, a reduction in cell voltage of 63 mV at 2 A cm⁻² was achieved in an AEMWE operating with 1 M KOH electrolyte. This improvement was enabled by the high internal surface area and the unique pore structure of the APS-MPL with a broad pore size distribution as well as the finely structured surface providing a large contacting area to the CLs.

This is an open access article under the terms of the Creative Commons Attribution-NonCommercial-NoDerivs License, which permits use and distribution in any medium, provided the original work is properly cited, the use is non-commercial and no modifications or adaptations are made.

© 2024 The Author(s). Electrochemical Science Advances published by Wiley-VCH GmbH.

1 | Introduction

In the de-fossilized economy of the future, green hydrogen produced via water electrolysis using renewable energy is expected to play an important role as an energy storage medium to buffer intermittently available green electricity sources [1]. Further, it will find use as a base chemical in existing industries [2], such as steel [3, 4] and ammonia production [5], and emerging industries such as synthetic fuels for aviation [6].

Anion exchange membrane water electrolysis (AEMWE) combines the low-cost materials traditionally used in alkaline water electrolysis (AWE) with the high efficiency zero gap configuration and solid ion-conducting electrolyte used in proton exchange membrane water electrolysis (PEMWE) [7–10]. Enabled by major strides in improving AEM conductivity and stability during the last decade [11], AEMWE is considered to be one of the most promising electrolysis technologies for large-scale deployment and is focused by many research groups, emerging start-ups and large companies worldwide.

However, besides high electricity cost, high electrolyser investment cost (CAPEX) is currently still holding back the economic appeal of all electrolysis technologies for hydrogen generation. Significant innovation and research effort to decrease investment and operational costs of electrolysers are needed to meet the ambitious goals set by national and trans-national agencies around the world [12, 13]. Within state-of-the-art (SoA) AEMWE stacks, metallic foams and felts, used as porous transport layers and/or micro porous layers (PTL/MPL), are currently the most expensive components, accounting for half of stack cost due to the high cost base material [14], typically high purity nickel, as well as their cumbersome manufacturing processes. The PTL/MPL has to balance several important tasks in the AEMWE. It is responsible for managing transport of electrolyte and liquid water to the catalyst layers (CLs), transport of evolving gas bubbles away from the CLs, and establishing thermal and electrical connection between the CLs and bipolar plates (BPPs) [15-18]. Furthermore, especially when the CL is directly deposited onto the MPL forming a catalyst-coated substrate (CCS), the MPL surface properties can significantly impact CL stability.

These aspects are highly consequential for electrolyser efficiency and durability, rendering the PTL/MPL not just one of the key cost-defining, but further one of the key performance-defining components in AEMWE, as it is also understood to be in PEMWE [18]. Within the overall efforts to improve AEMWE, developing novel PTL/MPLs with reduced material and manufacturing costs driving down CAPEX and optimized structural properties to improve electrolysis efficiency is thus a very worth-while approach. Nevertheless, only a handful of published studies have focussed on the PTL/MPL for AEMWE [15-17, 19, 20]. Some findings in regards to optimal PTL/MPL structure for PEMWE can be transferred to AEMWE, although fundamental differences affecting catalyst contacting and mass transport processes exist between these technologies. For one, the common use of high conductivity electrolyte in AEMWE leads to gas evolution within metallic PTLs/MPLs, which masks effects induced by MPL/CL interaction and might interfere with the mass transport into and out of the CL. For another, AEMWE electrodes are often prepared by directly coating PTLs/MPLs with catalyst instead of the catalyst-coated membrane (CCM) approach almost exclusively followed in PEMWE. To better understand the role of the PTL/MPL in AEMWE, further research that considers these circumstances is needed.

One of the most versatile, cost-efficient, and easily upscaled methods for depositing thick, dense or porous metallic coatings on a metallic substrate is plasma spraying. At the same time, plasma sprayed coatings are significantly less expensive than typical SoA MPLs, such as foams, felts or sintered sheets [21-23]. In contrast to vacuum plasma spraying (VPS), atmospheric plasma spraying (APS) does not require a large vacuum vessel, significantly reducing equipment investment costs and further increasing flexibility and scalability. Following this attractive calling, previous work was carried out, successfully developing plasma sprayed MPLs for PEMWE and AEMWE [16, 21-23]. Lettenmeier et al. produced stand-alone porous titanium MPLs for PEMWE via VPS introducing gradient pore size distribution, outperforming an SoA sintered titanium MPL at starkly reduced manufacturing costs [21]. Stiber et al. took a similar approach, but utilized a low-cost stainless-steel mesh PTL to directly deposit a thin and porous niobium/titanium MPL via APS, reaching performance equivalent to commercial sintered PTLs, with both reduced material and manufacturing costs [23]. Transferring the approach to pure water AEMWE, Razmjooei et al. coated the same mesh PTL with a porous nickel layer via plasma spraying, employing carbon as a pore forming agent. Compared to the uncoated mesh, performance was significantly improved by lowering contact resistances and improving mass transport [16].

In AEMWE a supporting alkaline electrolyte of varying conductivity is often employed to improve ionic connection to the catalyst [24, 25]. In fact, although advances have been made in regards to ionomer conductivity and stability, AEMWE operating with pure water does not yet achieve sufficient durability for an industrial use-case [26]. Employing an ionically conductive electrolyte opens up the possibility of circumventing the classical, fragile CL, including an ionomeric binder completely, as the liquid electrolyte itself, establishes the ionic connection between CL and AEM. Instead, an MPL with high inherent activity, high active surface area and structural properties that lead to efficient bubble removal from within its structure, then commonly dubbed porous transport electrode (PTE), can be employed. Following this concept, Wang et al. and Razmjooei et al. produced highly active and stable Raney-nickel and Raney-nickel/molybdenum electrodes via VPS and APS, reaching PEMWE-like performance [22, 27].

To improve upon previous developments and further the understanding of the role of the MPL in AEMWE at different operating conditions and with a supporting electrolyte, in this work we deposited a nickel based MPL on a mesh-type PTL substrate via APS. A continuous flat MPL akin to a sintered sheet was generated. This structural adjustment improves catalyst or AEM contacting and compatibility with fragile AEMs at high cell compression. To increase porosity and permeability, for the first time, a pore forming agent was included in the APS-layer, which was later removed in a separate step. Employing the developed APS-MPL in an AEMWE operating with 1 M KOH supporting electrolyte we report a significant performance improvement compared to an SoA nickel felt MPL (NF-MPL), when employed

2 of 20

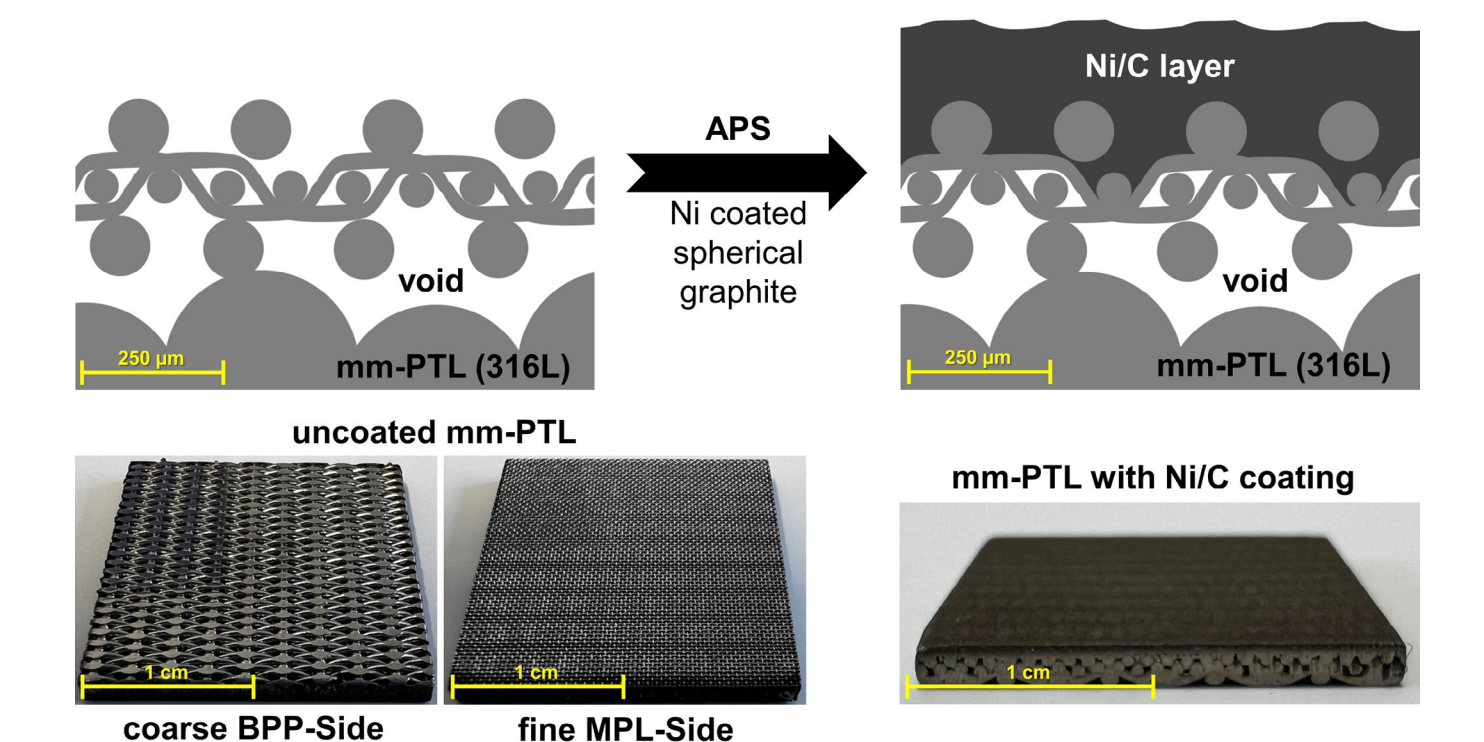


FIGURE 1 | Haver Porostar mm-PTL before (bottom left) and after APS coating (bottom right) and a scheme of the mm-PTL cross-section before and after Ni/C deposition (top). APS, atmospheric plasma spraying; mm-PTL, multi-mesh porous transport layer.

as a stand-alone PTE, as well as when used as a catalyst substrate (CS) in a CCS configuration. Moreover, we present the results of detailed chemical and structural analysis of the novel APS-MPL and elucidate the connection of chemical and structural properties and electrochemical behaviour in an AEMWE single cell.

2 | Methods

2.1 | Deposition of a Continuous Ni/C Layer on a Multi-Mesh PTL via APS

As PTLs and substrates for the deposition of the APS-MPL, 2×2 cm² 5-layer multi-mesh-laminate panels made from 316L stainless-steel (Porostar, Haver & Boeker OHG), with a 5 µm pore size dutch-weave wire-mesh as the finest mesh in the laminate, in the position second from the top in the laminate, were employed. The APS deposition process was carried out at ambient conditions and normal atmosphere. During the coating process, the plasma gun (Triplex-Pro210, Oerlikon-Metco) was fed with Ni-coated spherical graphite powder with an Ni:C weight-ratio of 60:40 and a particle size of <40 µm (E-Fill 2707, Oerlikon-Metco, $D90 = 30 \mu m$, $D50 = 20 \mu m$, $D19 = 14 \mu m$). Scanning electron microscopy (SEM) images of the feed powder can be found in Figure S1. The Ni/C APS-coating was prepared in 10 layers, using a robotic arm (IRB 4600, ABB) with a spray distance of 135 mm, step size of 5 mm and a raster speed of 400 mm s⁻¹. Gas flow rates were set to 80 NLPM Argon as primary gas and 10 NLPM helium as secondary gas. Deposition was carried out at 400 A, resulting in a total plasma power of 36 kW and a plasma enthalpy of approximately 11.5 MJ kg⁻¹. Excellent visual representations of the APS process can be found elsewhere [16, 22]. Before deposition, the mesh PTL substrates were preheated to 250°C. Figure 1 includes photographs of the Haver multi-mesh PTL (mm-PTL) and a scheme of the deposition process. Due to the small pore size and dutch-weave mesh style, the partly molten particles in the deposition zone do not penetrate the outer most meshes of the mm-PTL and quickly form a continuous layer.

2.2 | Processing of the Ni/C Layer to Produce the Ni APS-MPL

Figure 2 shows a scheme of the PTL/APS-MPL during the processing steps following the APS deposition of the Ni/C layer. Photographs of the PTL/APS-MPL after the processing steps can be found in Figure S2.

Due to the anisotropic porosity distribution over the Haver surface (MPL-side), the Ni/C layer surface exhibits a wave-like surface height distribution (Figure 1). To remedy this, after the APS deposition process, the Ni/C layer was ground first with 3000-, then with 7000-grid SiC paper creating a flat surface. Following, to remove the pore-forming agent C from the Ni/C layer, the individual 4 cm² PTL/MPL components were placed in a quartz tube open to normal atmosphere at both ends, exposing the samples to ambient air. The tube was inserted into a tube furnace and temperature was raised to 700°C. After exceeding 600°C ignition of the Ni/C layer was observed, as the C and Ni were quickly oxidized, burning in a blue flame (Figure S3). The furnace temperature was held at 700°C for 60 min in an effort to achieve complete C oxidation. Following, furnace temperature was lowered to 500°C while purging the quartz tube holding the samples with N_2 at 100 mL min $^{-1}$ for 15 min. Next, N_2 purge

26985977, 2025, 3, Down1

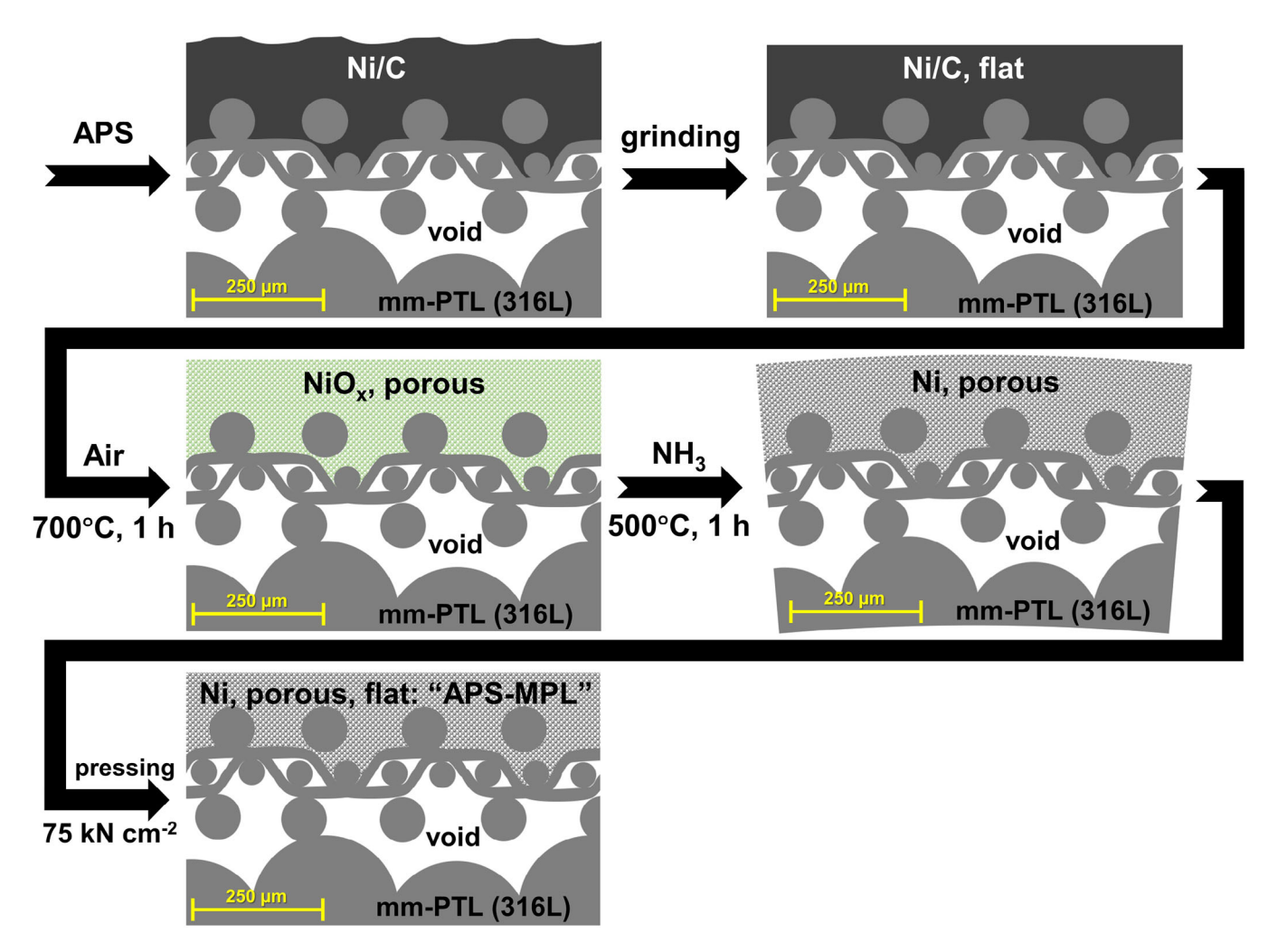


FIGURE 2 | Scheme of processing steps of the Ni/C APS layer after deposition, generating the porous APS-MPL. APS, atmospheric plasma spraying; APS-MPL, atmospherically plasma sprayed micro porous layer.

was stopped and a flow of NH₃ was started at 50 mL min⁻¹. The furnace temperature was held at 500°C for an additional 60 min to achieve complete reduction of any formed Ni oxides. Condensation of water was observed in gas flow direction at cold parts of the quartz tube, suggesting that a reduction reaction was indeed taking place. Subsequently, NH₃ flow was stopped, N₂ purge at 100 mL min⁻¹ was started again and the samples were allowed to cool down to room temperature inside the purged quartz tube. Slight bending of the PTL/APS-MPL components was observed after the reduction process. To flatten the samples, they were briefly pressed against Ni-coated steel plates at 75 kN cm⁻² in a hydraulic press. This reversed the bending to a large degree, although perfect flatness was not achieved.

Before installing the PTL/MPL in AEMWE cells or applying CLs, the PTL/MPL samples were thoroughly cleaned by ultrasonication in acetone, isopropyl alcohol and ultra-pure water, consecutively.

All mm-PTL/APS-MPL samples tested in this study were prepared in a single APS-deposition process as a joint component which was later separated into several 4 cm² pieces. By this, the impact of differences between spraying processes was excluded from this study.

2.3 | Synthesis of the Ni/Fe-LDH OER Catalyst

11.349 g nickel acetate tetrahydrate (99%, ChemPur) and 1.576 g iron nitrate nonahydrate powder (98% to 101%, Alfa Aesar) were dissolved separately to obtain a 76 mL 0.6 M nickel acetate and a 6.5 mL 0.6 M iron nitrate precursor solution. For the synthesis, the prepared nickel acetate solution is first mixed with 216 mL of DMF and stirred for 30 s. Then, while continuously stirring, the prepared iron nitrate solution is added to the mixture. The solution is further stirred for 24 h. After 24 h, 144 mL of DMF and 250 mL of Milli-Q water are added. For the next step, a microwave (Anton Paar, Masterwave BTR)-assisted synthesis procedure is conducted, applying a temperature protocol previously published [28, 29]. To reliably reach the desired Ni/Fe ratio in the final synthesis product, heating rates of the reaction mixture are high and tightly controlled. The reaction solution is heated to 120°C as quickly as possible, within 90 s. The temperature is then held constant for 60 min. Next, the solution is further heated to 160°C as quickly as possible, within 120 s. The temperature is then held constant for another 30 min. Finally, the solution is cooled to 55°C. After the synthesis, the slurry is centrifuged at 8000 rpm for 15 min. The supernatant is then removed. The precipitated catalyst is then dispersed, washed and centrifuged (15 min at 8000 rpm) in 200 mL of Milli-Q, EtOH and Mili-Q. The final

product is frozen with liquid nitrogen for 30 min. It is then dried in a freeze dryer at -45° C under vacuum for 3 days.

2.4 | Deposition of CLs on the MPLs via Spray-Coating

Catalyst inks were prepared by first ultrasonically dispersing 50 mg of catalyst powder in 10 mL of ultra-pure water (MiliQ, 18 M Ω cm $^{-1}$) for 30 min, followed by the addition of 10 mL isopropyl alcohol (ACS reagent, \geq 99.5%) and additional ultrasonic dispersion for 30 min. Then, 250 mg of a 5 wt.% ethanolic Piperion ionomer solution (Versogen) was added. Finally, the inks were ultrasonically dispersed for a final duration of 10 min.

Ultrasonic dispersion took place at 20°C, in a Bandelin Sonocool ultrasonic bath set to 50% and 100% power for preparing the Pt/C catalyst ink and the Ni/Fe-LDH catalyst ink, respectively. A lower power setting was used for the Pt/C ink to limit Pt detachment.

Catalyst inks were directly deposited on the reference NF-MPL and the developed PTL/APS-MPL samples, creating CCSs. Deposition was carried out using a lab-made automatic airbrush spray-coating device. Ink was deposited with a nozzle distance of 5 cm at a rate of 0.5 mL min-1. The CSs were heated to 60°C during the deposition process. Figure S4 shows photographs of the APS-MPL and NF-MPL before and after the deposition of the Pt/C cathode CL. To ensure that the cell test results were not impacted by batch-to-batch variation of the catalyst inks or differences in coating parameters, the anode CLs and cathode CLs of all tested samples were deposited simultaneously in a single deposition session using a single batch of ink. Figure S5 shows the substrate configuration employed for spray deposition. The mass of the coated substrates was carefully determined to control the achieved loading. In all cases, the difference between target loading and achieved loading was smaller than $\pm 5\%$.

2.5 | Physical Characterization

2.5.1 | Scanning Electron Microscopy/Energy Dispersive X-Ray Spectroscopy (SEM/EDX)

All surface imaging, cross-sectional imaging and EDX operations were performed using a Zeiss Crossbeam 350 FE-SEM equipped with an EDS Detector (Oxford ULTIM MAX 100 mm²). Imaging was performed at a working distance (WD) of 5 mm and 2 kV accelerating voltage. EDX mapping operation was performed at a WD of 5 mm and an accelerating voltage of 15 kV averaging five images. To generate large area cross sections, samples were cut for 12 h without any embedding using Jeol Ion Cross Section polisher with 6 kV for generating the Ar-ion beam at room temperature while the stage was swinging.

Focused Ion Beam- (FIB-) SEM tomography: To visualize the porous structure of the MPL in 3D, both gallium-FIB (Ga-FIB) and Plasma FIB (PFIB) were used.

Gallium FIB-SEM tomography: The Zeiss Crossbeam 350 FE-SEM equipped with gallium liquid metal ion source was utilized for this purpose. FIB operations were performed at a WD of $\sim \! 5.1$ mm at the coincidence point of the electron and ion beam at 54° sample tilt. A slicing current of 1.5 nA at 30 keV was employed throughout the slicing process with drift correction enabled due to 3D tracking marks prepared before with a platinum and carbon gas injection system. Secondary electron (SE) imaging was conducted using an Everhart-Thornley (E-T) detector with a dwell time of 0.4 μs with a line average of 10, an imaging current of 231 pA and an accelerating voltage of 2 keV. A total slice count of 1418 slices with pixel and slice size of 10 nm was taken. The images were exported with Zeiss Atlas 5 TrueZ function to receive exactly 10 nm each slice.

PFIB -SEM tomography: PFIB-SEM tomography was carried out using a Xenon PFIB (TESCAN, Amber X). The sample was firmly attached to a SEM stub with Conductive Carbon Cement to prevent any movement during tomography. The FIB milling was performed at a WD of 6 mm, aligning the electron and ion beams at the intersection point, with a sample tilt of 55°. A slicing current of 50 nA at 30 keV was employed, along with drift correction to ensure accurate alignment throughout the slicing process. SE imaging was conducted using an E-T detector with a dwell time of 3 µs, an imaging current of 300 pA and an accelerating voltage of 2 keV. Imaging was performed with a pixel size of 50 nm, and the slice thickness was set to 100 nm. A total of 1269 slices were acquired during the procedure.

2.5.2 | Micro Computer Tomography (μCT)

The μ -CT analysis was performed with the x-ray microtomograph SkyScan 1172 (Bruker) with an acceleration voltage of 80 kV and a current of 100 mA. Scans were carried out with an optical resolution of approximately 2 μ m per pixel, 180° rotation and a rotation step of 0.2°.

2.5.3 | 3D-Reconstructions and Calculation of Structural Parameters Based on µCT, FIB-SEM and PFIB-SEM Data

The segmentation of the greyscale data obtained by μCT and FIB-SEM, as well as the calculation of structural and transport parameters were carried out using GeoDict (GeoDict Version 2024 Math2Market GmbH). A brightness gradient correction was generally performed before segmentation; In the case of the SEM data, a curtaining filter was additionally applied. The resulting data set was subsequently segmented using the AI model UNet 3D contained in GeoDict. This method was best suited for the MPL case to differentiate among nickel, carbon and pore space, while neglecting typical shine-through artifacts of the greyscale images. Structural parameters like porosity and pore size distribution were received using the packages MatDict and PoroDict. For determining transport parameters and the capillary pressure curves, the packages DiffuDict, ConductoDict and SatuDict were used. Material parameters were obtained from the GeoDict material database. An estimated contact angle of 45° between 1 M KOH and Ni in oxygen atmosphere was employed

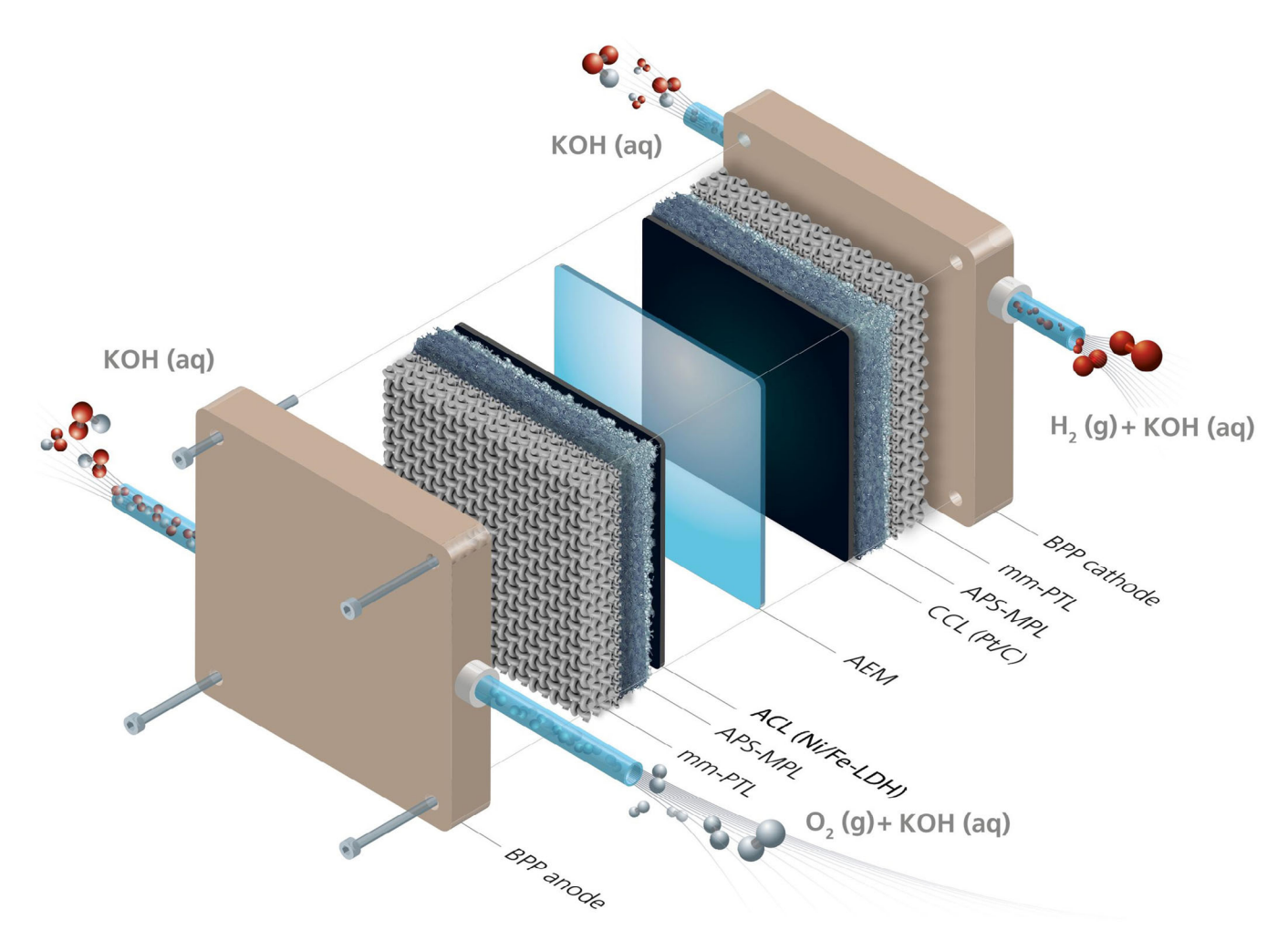


FIGURE 3 | Scheme of the AEMWE single-cell using the mm-PTL/APS-MPL in a CCS configuration on both anode and cathode. APS-MPL, atmospherically plasma sprayed micro porous layer; CCS, catalyst-coated substrate; mm-PTL, multi-mesh porous transport layer.

for the simulation of l/g distribution and capillary pressure in the MPLs.

2.5.4 | Atomic Force Microscopy (AFM)

With an Icon XR from Bruker PF-TUNA conductive tapping was performed using conductive (doped) diamond AFM tips (DDESP-V2, Bruker). Image size was chosen to be 25 \times 25 μm^2 with a resolution of 1024 pixels. The bias was maintained at 500 mV for all samples which were glued to 125 mm sample pucks with conductive carbon tape.

2.5.5 | X-Ray Diffraction (XRD)

XRD was performed on a D8 ADVANCE (Bruker AXS GmbH, Germany) to analyse the phases of the samples. A parallelized Cu $K\alpha$ x-ray source was used as the incident beam ($\lambda=1.54178$ Å, 40 kV—40 mA). An equatorial Soller slit (0.41°) was used with a LYNX-EYE XE-T detector operated in 0D—high-energy resolution mode to record diffractograms by $2\theta-\theta$ scan.

2.5.6 | Mercury Intrusion Porosimetry (MIP)

The pore size distribution of the Haver mm-PTL and PTL/APS-MPL was determined by MIP up to a pressure of 200 MPa (Pascal 140/240, Thermo Scientific). The dimensions of all samples tested were approximately $2 \text{ cm} \times 2 \text{ cm}$.

2.6 | AEMWE Single Cell Characterization

A scheme of one of the cell configurations used for the single-cell experiments in this study is shown in Figure 3.

Titanium grade 1 BPPs and 316L stainless-steel mm-PTLs (Porostar 5-layer, Haver & Boeker) were used on both anode and cathode. As MPL, either the reference Ni felt (NF-MPL) or the MPL deposited on the PTL via APS (APS-MPL) was used. The MPLs were both tested as stand-alone PTEs as well as in combination with low loading CLs, directly deposited onto the MPLs. The AEM (100 μ m DURAION AEM, Evonik) and CCSs were activated by submersion in 1 M KOH at 60°C for 1 h, exchanging the activation solution once after 30 min, followed by storage in fresh 1 M KOH overnight. The cell assembly was compressed using four

bolts, reaching an effective compression over the active area of the cell of 130 N cm⁻². Testing was performed at 70°C, feeding 1 M KOH to both anode and cathode via natural convection. Before the recording of the polarization curves and electrochemical impedance spectra (EIS), the cell voltage was cycled between 1.3 and 2.0 V for 3 h for conditioning. As per recommendations of the Joint Research Centre of the European Commission (JRC), the cells were held at 100 mA cm⁻² for 5 min before commencing the polarization curve measurement [30]. Polarization curves were recorded step-wise, increasing current density from 2.5 mA cm⁻² to maximum current density, before stepping back down. Dwell time was 30 s at 2.5, 5 and 10 mA cm⁻² and 10 s at all other operation points. Cell current and potential were recorded for 10 s at each step following the dwell time. Values of cell current and cell potential for each step in the polarization curve are the result of forming an average of data recorded during these 10 s of measurement time. Following the polarization curve, EIS were recorded at 0.1 A cm⁻² and 1 A cm⁻² with an amplitude of 5 and 10 mV, respectively, using a Zahner Elektrik IM6 potentiostat with a booster module (Zahner Elektrik PP241). Before each EIS, the cell was allowed to stabilize for 10 min.

3 | Results and Discussion

3.1 | MPL Structure During the Manufacturing Process

In previous work, the MPLs and electrodes generated for AEMWE via plasma spraying were of a non-continuous nature, following the height profile of the mesh substrate, leading to a very rough MPL surface, potentially damaging to the thin AEM [16, 22]. Further, large openings at the mesh remained in the MPL surface, leading to areas without contact to the AEM or CL, likely reducing catalyst utilization and overall cell performance. In an effort to remedy both issues, in this work, a continuous, flat and smooth MPL, akin to a sintered sheet with a small particle and pore size was developed. This was achieved by utilizing a PTL substrate with a small aperture dutch weave mesh. The deposited MPL quickly closed the mesh completely, creating a continuous top surface. In contrast to the previously developed plasma sprayed MPLs, large mesh openings can no longer facilitate fast removal of generated gases. Instead, all gas is transported directly through the continuous MPL itself. This task requires an MPL with high permeability, a requirement that is not easily achieved via plasma spraying of pure metallic powders. Instead, this was done by including C as a pore-forming agent in the APS process. Employing an Ni-coated spherical graphite powder, a continuous porous Ni matrix filled with C was deposited. In a second manufacturing step, the C was removed by oxidation in air, leaving behind a porous NiO structure. The formed NiO was converted back to metallic Ni through reduction in an NH3 atmosphere, generating the final APS-MPL structure, which shows sufficiently high permeability, due to a high porosity and large primary pores, as seen in Figure 4.

The images of SEM/EDX of the surface and ion-cut cross-sections of the APS-MPL throughout the preparation process are found in Figures S6 and S7, respectively. The initial Ni/C APS-layer, deposited in 10 layers, has a thickness of approximately 400 μ m. The EDX analysis of cross-sectional images reveals a

layer composition of approximately 70 vol% C and 30 vol% Ni, which is in agreement with the feed powder composition. This suggests no preferential loss of a single component, that is, C or Ni took place during the APS process, for example, via sublimation or oxidation. The internal layer structure is free of oxides, whereas on the top surface a small but detectable oxygen signal was registered locally. This was likely caused by the prolonged air contact of the hot top-surface of the coating after deposition had ended. The absence of any oxides within the layer structure can be explained by the reducing action of C, as well as the local inert noble gas atmosphere generated during the APS. The morphology of the Ni and C phases in the deposited layer shows resemblance with the feed powder (SEM image in Figure S1). Notably, the C phase is made up of large close-to-spherical features, whereas the Ni phase fills the space between. The Ni phase is highly heterogeneous, showing both large features at around 10 µm size as well as very small features at <1 µm size. Furthermore, larger Ni features include small particles of locked-in C at micrometre and sub-micrometre size. The porosity of the Ni/C layer is close to zero. Subsequent sanding of the Ni/C layer with 3000- and 7000grid SiC paper generated a level, flat and smooth surface. The following oxidation in air successfully removed the vast majority of the C phase, accompanied by the oxidation of the Ni matrix. Elemental ratios determined via EDX suggest total oxidation to NiO, aside from small regions in the centre of the largest Ni features. The Ni oxidation was accompanied by a volume increase of the Ni-based phase, partly closing the pores left behind by the C phase, leading to a porosity reduction (estimated on the basis of binarized SEM micrograph, Figure S8A). SEM images at high magnification of the layer surface reveal small crystallites of NiO as well as small pores that are formed during oxidation of encapsulated C. Subsequent reduction in NH₃ led to a shrinkage of the Ni-based phase, increasing porosity (estimated on the basis of binarized SEM micrograph, Figure S8B). The EDX analysis shows that a complete reduction of NiO to metallic Ni took place. Finally, the pressing step significantly reduced layer porosity once again (estimated on the basis of binarized SEM micrograph, Figure S8C) and flattened the top-most surface features, partly closing the sub-micrometre secondary pores. The final average thickness of the APS-MPL is approximately 250 µm. Locally resolved surface conductivity measurements were carried out via AFM (Figure S9). Notably, these measurements corroborate the assumption of total conversion of Ni to NiO during the oxidation step, as the surface of the APS-layer shows very low conductivity in the oxidized state.

3.2 | Structural and Chemical Analysis of the APS-MPL

Before physical characterization, the easily irreversibly deformed NF-MPL was compressed at 130 N cm⁻² to simulate cell conditions. Figure 4 shows SEM images including EDX maps of the surface and ion-cut cross sections of the MPLs tested in this study, the SoA NF-MPL (Figure 4A) and the novel APS-MPL deposited on the mm-PTL (Figure 4C-H). EDX and XRD analysis (Figure S10) reveals, that like the SoA NF-MPL, the APS-MPL is made up of elemental Ni, with some remaining C and an almost undetectable amount of oxygen, which only appears locally on the top surface of the APS-MPL in EDX (Figure 4C), but is not detected via XRD. Functionally, the APS-MPL can be considered

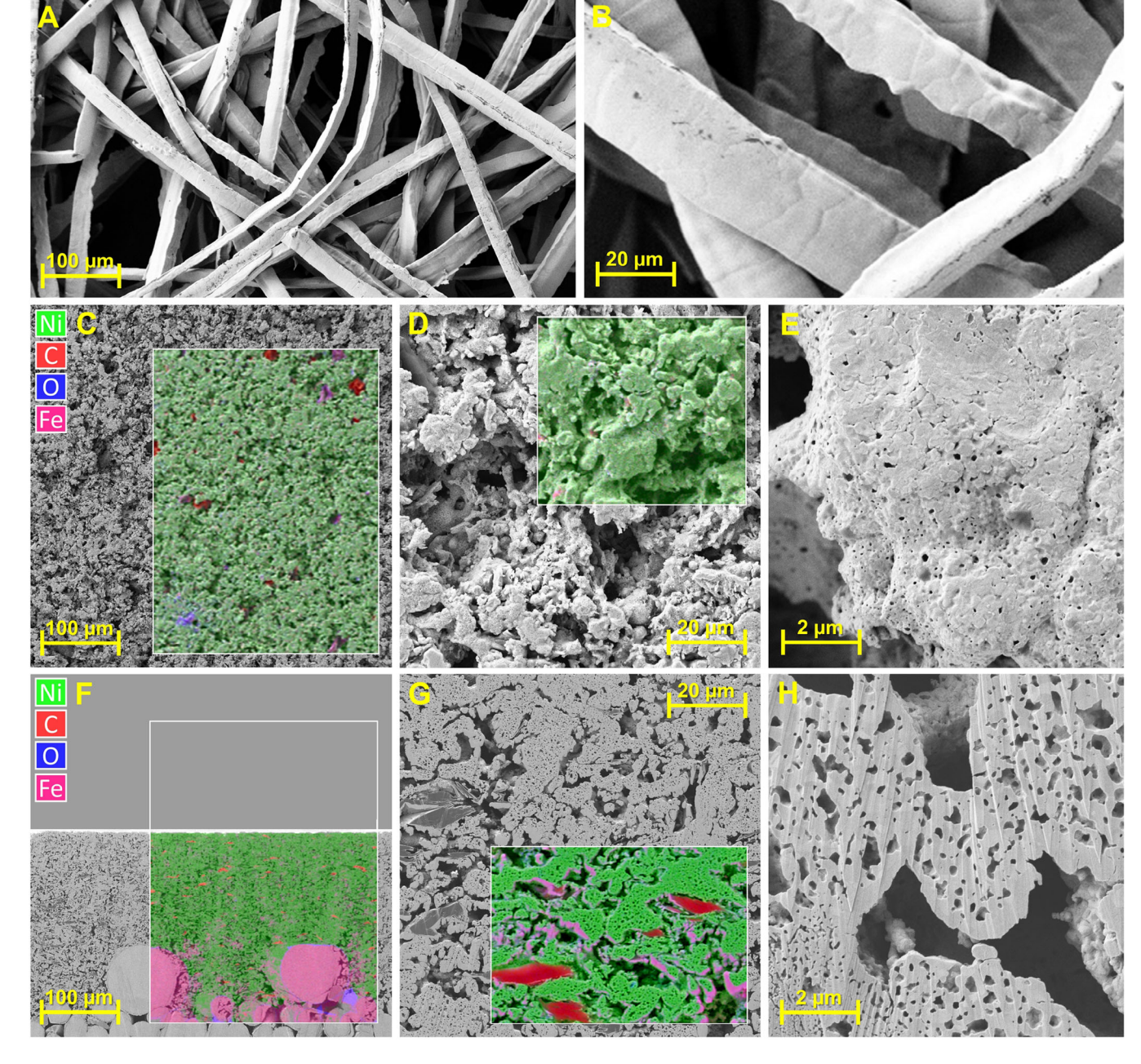


FIGURE 4 SEM/EDX of the surface of the NF-MPL (A, B) and APS-MPL (C-E) and SEM/EDX of ion-cut cross sections of the APS-MPL (F-H). APS-MPL, atmospherically plasma sprayed micro porous layer; NF-MPL, nickel felt micro porous layer; SEM/EDX, scanning electron microscopy/energy dispersive x-ray spectroscopy.

to be a pure metallic Ni structure. Iron detected in the APS-MPL in the cross-sectional EDX mappings was introduced by the ion-cutting process itself due to the steel shielding plate and does not reflect the presence of Fe in the pristine APS-MPL (Figure 4F). In contrast to the NF-MPL, which consists of Ni fibres with a diameter of approximately 20 μm , the APS-MPL resembles a porous sintered sheet of irregularly shaped particles of smaller and more diverse size connected via melting and interdiffusion during the APS process and/or sintering during post-processing. Due to the relatively high diameter and low packing density of the Ni fibres, the porosity and surface roughness of the NF-MPL is significantly higher compared to the APS-MPL. Thereby, the APS-MPL is less likely to cause damage to the AEM, as clamping forces

are distributed more homogeneously. Furthermore, the NF-MPL shows a significant open area, caused by large pores completely penetrating the NF-MPL, whereas the APS-MPL is continuous. Thus, large areas of the CL will likely remain inactive, when employing the NF-MPL in a CCM scenario. This effect is also expected when using previously developed VPS and APS MPLs, where the top mesh of the PTL substrate remained open [16, 22]. In contrast, the APS-MPL developed in this study will provide a larger contacting surface, more uniform pressure distribution and higher density of contact points—features that improve catalyst utilization and CL stability [31]. Whereas the surface of the individual Ni fibres of the NF-MPL is smooth, not showing any pronounced structuring (Figure 4B), the surface of the APS-MPL

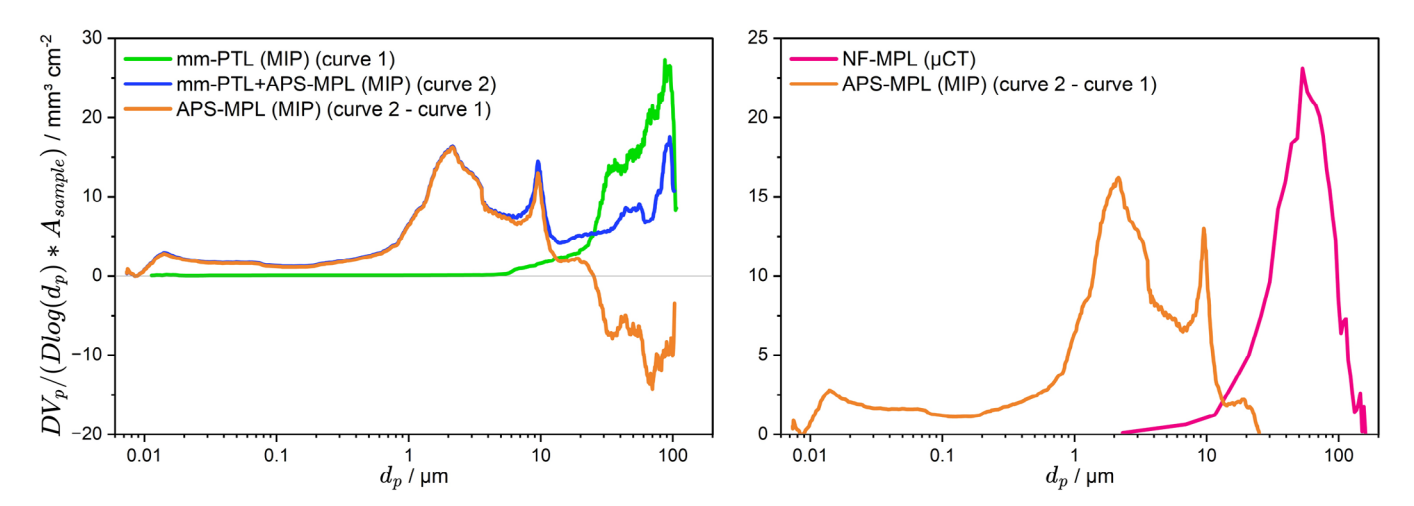


FIGURE 5 Differential area–specific pore size distribution of mm-PTL, mm-PTL with APS-MPL, APS-MPL and NF-MPL, based on MIP and μCT data. μCT, micro computer tomography; APS-MPL, atmospherically plasma sprayed micro porous layer; MIP, mercury intrusion porosimetry; mm-PTL, multi-mesh porous transport layer; NF-MPL, nickel felt micro porous layer.

seemingly exhibits high rugosity, caused by the highly irregular shape and diverse size of Ni features in the coating (Figure 4D). In a CCS setting, this significant increase in rugosity will likely improve CL adhesion by increasing the area over which binding forces can act.

As previously stated, imaging of the ion-cut cross sections of the APS-MPL reveals that the primary Ni skeleton of the APS-MPL contains a high number of sub-micrometre secondary pores that first and foremost were formed by the oxidative removal of small C inclusions in the Ni/C layer (Figure 4H). However, the number of these small secondary pores seems to increase during the reduction of the oxidized Ni layer, suggesting a connection to the solid volume loss during conversion of NiO to Ni. Fundamental studies on the NiO reduction process have reported the occurrence of porous phases [32]. Surface imaging of the APS-MPL at very high magnification reveals sub-micrometre pore openings, suggesting that some of the small secondary pores are accessible and connected to the primary porous network (Figure 4E). In a CCS setting, the intrusion of catalyst ink into the sub-micrometre pores open to the surface might lead to a form-fit connection between CL and MPL, further improving CL adhesion, compared to the NF-MPL.

To quantify and compare the structural properties of the MPLs, μ CT, MIP, Ga-FIB-SEM and PFIB-SEM were carried out. Figure 5 presents the porosimetry results of both MIP measurements and μ CT analysis. Due to the large and non-spherical pores in the NF-MPL, in this case μ CT is the more suitable technique to produce meaningful results. On the basis of the μ CT and MIP data, the following observations are made:

1. Besides the larger pores within the large aperture size mesh on its backside that cannot be detected by MIP, the mm-PTL does contain pores in a size range of 10–100 μm . Pores at $\sim\!100\,\mu m$ can be assigned to the top-most and third-from-thetop square meshes with an aperture size of approximately 100 μm , whereas the smaller pores can be assigned to the tight dutch-weave mesh, second from the top. On the basis of the MIP, the deposition of the APS-MPL closes approximately

50% of these pores. This correlates well with the appearance of the APS-MPL cross-sections, as the APS-MPL penetrates and fills the top half of the surface structure of the mm-PTL. This is especially visible in a cross-sectional SEM micrograph that includes the mesh structure of the PTL (Figure S11).

- 2. Below 10 μ m diameter, all pores of the PTL/APS-MPL sample can be assigned to the APS-MPL itself, as the mm-PTL does not seem to contain pores with a smaller pore diameter.
- 3. Compared to the NF-MPL, which contains large pores between 10 and 100 μm with a distinct PSD maximum at $\sim 50~\mu m$, the average pore size in the APS-MPL is much smaller and its PSD is significantly broader.
- 4. The APS-MPL contains pores of 10 nm to 20 µm diameter. Pores in the size range of 25–1 µm, with local PSD maxima at 20, 10 and 2 µm can mainly be assigned to the primary porous APS-MPL network, whereas the pores with smaller diameter, with a local PSD maximum at 20 nm, can be assigned to the secondary pores within the primary Ni skeleton. It should be noted that due to the nature of the MIP process pores are detected on the basis of their throat size. The significant pore volume detected at pore throat diameters between 0.02 and 0.1 µm might therefore be connected to larger pores within the secondary pore network, which are connected through very narrow throats. This assumption fits well with the impression given by the cross-sectional images discussed earlier, as here, most of the secondary pores seem to be around 0.1 µm in diameter and not many appear to be smaller than 0.1 µm in diameter.

Besides the chemical make-up, qualitative structural aspects and pore size distribution that were determined via SEM/EDX, XRD, μ CT and MIP, additional structural parameters that are thought to be most relevant to this study are porosity, through-plane and in-plane tortuosity ($t_{\rm thr-pl}$, $t_{\rm in-pl}$), volume ratio of closed pores ($V_{\rm p,cl}/V_{\rm p,total}$) and specific surface area per geometric MPL area (SSA). To determine these additional structural parameters that impact the electrochemical behaviour of the MPLs in a PTE, CCS or CCM setting, 3D-reconstructions based on μ CT data of the

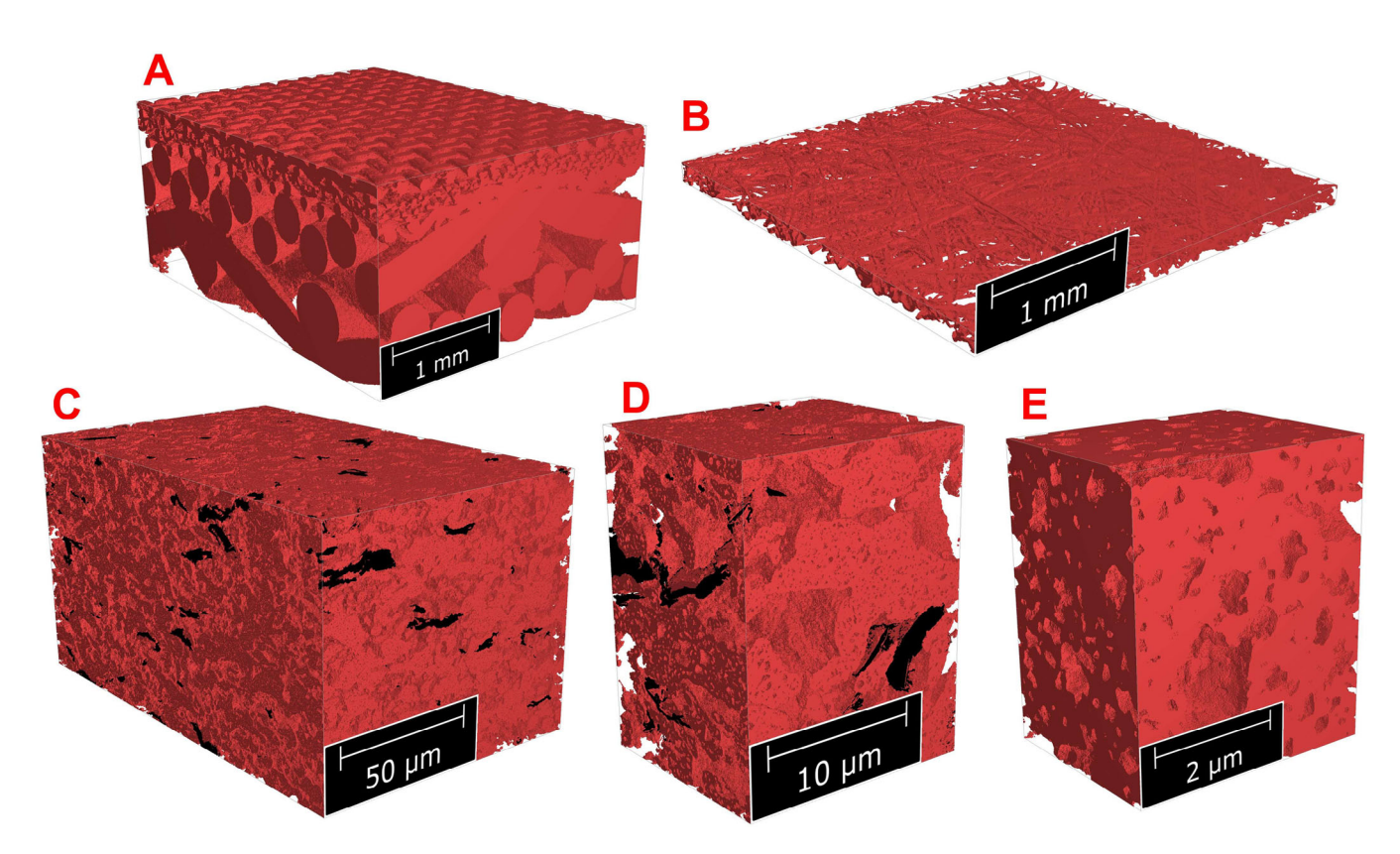


FIGURE 6 | 3D-reconstructions of the mm-PTL (A) and NF-MPL (B) based on μ CT data and 3D-reconstruction of the APS-MPL based on FIB-SEM imaging at increasing magnification levels (C–E). At highest magnification, only the secondary pore network is visible (E). The red and black phases correspond to Ni and C, respectively. μ CT, micro computer tomography; APS-MPL, atmospherically plasma sprayed micro porous layer; FIB-SEM, focused ion beam-scanning electron microscopy; mm-PTL, multi-mesh porous transport layer; NF-MPL, nickel felt micro porous layer.

TABLE 1 | Structural parameters of the micro porous layers (MPLs) characterized in this study.

	p (%)	t _{thr-pl} /-	<i>t</i> _{in-pl} /-	$V_{ m p,cl}/V_{ m p,total}$ (%)	SSA/ $m^2 m_{geo}^{-2}$
APS-MPL (PFIB-SEM), complete structure	44.1	3.8	3	11.1	382
APS-MPL (PFIB-SEM), primary structure	39.1	3	2.7	0.0	211
APS-MPL (Ga-FIB-SEM), secondary structure	26.4	61.9	104.1	5.9	1284
NF-MPL (μCT)	74.3	1.53	1.4	0.0	6.6

Note: For the calculation of the specific surface area (SSA), an MPL thickness of 200 µm was assumed.

Abbreviations: µCT, micro computer tomography; APS-MPL, atmospherically plasma sprayed micro porous layer; Ga-FIB-SEM, gallium-focused ion beam-scanning electron microscopy; NF-MPL, nickel felt micro porous layer; PFIB-SEM, plasma focused ion beam-scanning electron microscopy.

NF-MPL, and Ga-FIB-SEM and PFIB-SEM data of the APS-MPL were analyzed. 3D-reconstructions of the MPLs and the mm-PTL are found in Figure 6.

Table 1 includes the determined calculated values of selected structural parameters. To gain insight into the differences between the primary and secondary pore networks, in one analysis the small pores of the secondary pore network were disregarded ("primary structure"), whereas in another, only a small sample volume containing a section of the secondary pore network was analysed ("secondary structure", Figure 6E).

The apparent lower porosity of the APS-MPL, compared to the NF-MPL, is reflected in the numerical values determined on the basis of PFIB-SEM and μ CT reconstructions, at 44.1% and 74.3%, respectively. It should be noted that in the APS-MPL processing,

the final pressing step employed to flatten the samples could be easily circumvented by fixing the PTL/MPL on a rigid holder, preventing bending during the reduction in NH₃. This would increase the final porosity of the APS-MPL significantly, likely to values higher than 50%. This is distinctly higher than what was previously achieved using plasma spraying to prepare MPLs or electrodes [16, 21–23]. This step-up in porosity was made possible by using the pore-forming agent and its subsequent removal and leads to increased permeability and likely to improved mass transport management in the AEMWE cell. The tortuosity of the APS-MPL is equal to 3.8 and 3 in through- and in-plane direction, respectively, which is higher than the tortuosity of sintered or fibrous structures used in commercial electrolysers, where tortuosity is typically between 1.2 and 2 [33, 34]. The high tortuosity of the APS-MPL is induced by the still comparably low porosity after the pressing step and complex structure,

including small secondary pores. The tortuosity of the APS-MPL is anisotropic due to the directionality of the APS process, resulting in a flattening of pores and particles parallel to the coating substrate. However, both magnitude and anisotropy of the tortuosity of the APS-MPL are reduced compared to the typical porous plasma sprayed layer prepared without a pore forming agent [21]. The preparation of porous metallic coatings without the use of a pore forming agent via plasma spraying is principally achieved by reducing the degree of melting of the particles, aiming to induce adhesion between particles without closing the gaps between. Achieving sufficiently high porosity and low tortuosity without compromising layer stability can be challenging, especially when a small particle and pore size (~10 μm) is targeted, which is preferable for an MPL. The inclusion of the pore forming agent and subsequent removal decouples layer porosity and pore structure properties from the degree of melting induced during the APS, increasing the achievable porosity at low pore size without compromising layer stability. Here, as seen in SEM images and as reflected in the PSD, the graphitic carbon pore former creates a unique, high porosity, multi-modal structure, including a large number of sub-micrometre secondary pores within the primary Ni structure, with a high internal surface area of 382 m² m_{geo}⁻², approximately 50 times higher than the SSA of the NF-MPL. Separate analysis of the primary and secondary pore structure reveals stark structural differences (Table 1). The pores of the primary structure are readily accessible and well connected, similar to the pores in a porous sintered structure, albeit with slightly higher overall tortuosity. In contrast, the secondary pore structure within the primary nickel skeleton shows extremely high tortuosity of up to 100 at an overall porosity of 26.4%. This suggests that the individual pores in the secondary pore structure are poorly connected through only a small number of narrow pore throats, leading to an ant-nest-like structure. This impression fits well with earlier observations based on MIP data, where intrusion into the secondary pore network was seemingly limited by narrow pore throats. During operation in an AEMWE cell employing conductive electrolyte, where significant gas evolution takes place on the MPL structure itself, it is likely that the extremely high tortuosity leads to insufficient water and electrolyte transport into the secondary pore network, rendering it gas filled and partly inactive. It should be noted that the (100 nm)3 voxel size of the PFIB-SEM 3D reconstructions, which was merely chosen to enable the analysis of a large sample volume in a short time frame, was seemingly not sufficient to resolve the pore throat channels in the secondary pore network. Thus, a large part of this porous network was determined to be closed. In contrast, analysis of a considerably smaller sample volume based on Ga-FIB-SEM data with a (10 nm)³ voxel size did not reveal a high number of closed pores. On the basis of this, as well as the pore openings visible in SEM surface images (Figure 4E) and the significant pore volume at $p_{\rm d}$ < 0.5 µm based on MIP data (Figure 5), it can be concluded with high confidence that in fact a large majority of secondary pores are both interconnected and connected to the primary pore network.

Through our multimodal characterizing approach comprising MIP, μ CT, Ga-FIB-SEM and PFIB-SEM tomography, detailed structural information of the novel APS-MPL and SoA NF-MPL was generated. Significant differences in all relevant structural parameters between these MPLs have been revealed. The SoA NF-MPL shows very high porosity, a large average pore size

and narrow pore size distribution, leading to high permeability and low capillary pressure, as well as a low-contact area, high roughness but low rugosity surface. In contrast, the novel APS-MPL shows lower, but sufficient porosity, smaller pores and a broad pore size distribution, leading to decreased permeability and increased capillary pressure, as well as a high-contact area, low roughness but high rugosity surface. In this, the APS-MPL is expected to increase CL utilization through improved CL contacting and improved mass transport management compared to the SoA NF-MPL.

3.3 | Numerical Simulations

The gas/liquid transport inside a porous MPL is a complex process that cannot be accurately numerically predicted in a way that makes real experiments redundant [35]. This is especially true in the present use case, where the use of a highly conductive electrolyte leads to gas evolution inside the MPL structure as well as in the supported CL. Nevertheless, certain numerical calculations can provide meaningful results that can advance the understanding of mass transport behaviour in MPL, both qualitatively and quantitatively.

Here, the drainage of a wetting phase due to the invasion of a non-wetting phase (oxygen gas) was simulated as a function of gas pressure. The results are shown in Figure 7. It should be noted that the secondary pore structure was not included in these calculations.

Throughout all saturation conditions, a considerably higher, approximately 50-fold pressure is needed for oxygen intrusion into the APS-MPL compared to the NF-MPL, due to the much smaller average pore size, leading to higher capillary pressure. Further noticeable is a higher range in intrusion pressure for the APS-MPL, which correlates with the broader pore size distribution. The effect of the broad pore-size distribution and local pore size inhomogeneities is visible in the gas/liquid distribution in the APS-MPL included in Figure 7. As a result of these features, at lower gas pressure preferential pathways for gas intrusion are established, whereas only at very high pressure, the complete pore structure is slowly filled with gas. This can be advantageous during AEMWE operation, as a complete displacement of the wetting phase is shifted to higher gas evolution rates, as some pathways might remain liquid filled longer, compared to a homogeneous porous structure.

3.4 | Electrochemical Characterization of the APS-MPL in a PTE and CCS Scenario in an AEMWE Single Cell Employing 1 M KOH Supporting Electrolyte

3.4.1 | Inherent Activity of the MPL in AEMWE

In alkaline AEMWE, due to the use of highly conductive electrolyte, all components in the cell compartments act as part of the electrodes when polarized. In this, porous structures made from active materials such as Ni and stainless-steel employed as PTL and/or MPL can contribute significantly to overall electrode performance. Thus, evaluating the ability of the novel APS-MPL

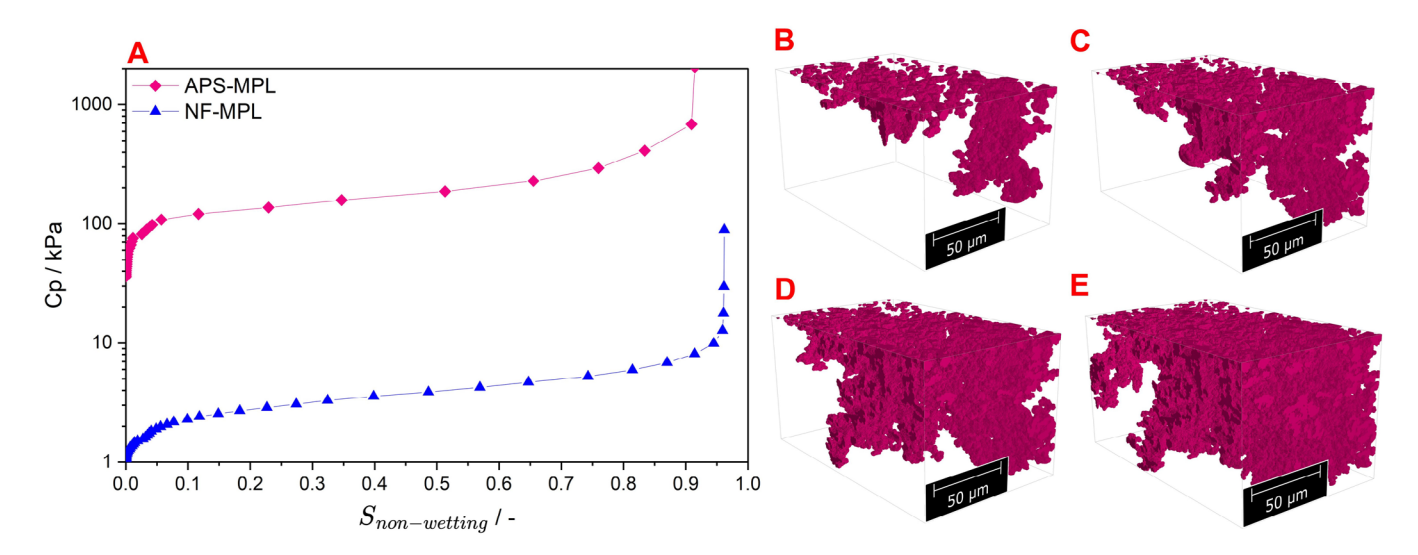


FIGURE 7 | Simulated intrusion of oxygen into the NF-MPL and APS-MPL as a function of gas pressure, starting at liquid-saturated conditions. (A) Capillary pressure curves, (B–E) Oxygen distribution in the APS-MPL at 10, 20, 30 and 40 vol% oxygen saturation. APS-MPL, atmospherically plasma sprayed micro porous layer; NF-MPL, nickel felt micro porous layer.

to improve catalyst utilization in a CCS or CCM setting compared to an SoA material at alkaline AEMWE conditions (1 M KOH to anode and cathode, 70°C) is challenging, as the characterization results will reflect both changes in inherent activity of the MPL and effects of modified catalyst contacting and mass transport. In an effort to separate these effects, the MPLs characterized in this study, the APS-MPL and the SoA NF-MPL were tested both as stand-alone PTEs, as well as in combination with low loading CLs, in a CCS setting.

3.4.2 | Cell Resistance Contributions and Separation via EIS

In water electrolysis at least four distinct separate cell resistance contributions can be identified by impedance analysis: (1) ohmic resistance, or high frequency resistance (HFR), as the sum of electronic and ionic resistances in the cell, (2) resistance towards the hydrogen evolution reaction (HER) on the cathode, (3) resistance towards the oxygen evolution reaction (OER) on the anode and (4) resistance related to the effect of mass transport processes [36-38], notably diffusion of dissolved gases at the electrode surface [39, 40], diffusion of water and gases in the ionomer phase of the CL [41], gas bubble evolution on the electrode surface and membrane surface leading to blockage and/or local reactant starvation [42, 43] and, when a supporting electrolyte is responsible for ion transport, displacement of the ion conducting phase by gases filling the porous electrode structure [42, 43]. The electrocatalytic and mass transport processes involve the accumulation of charge in the electrode double layer and the accumulation of gas or dissolved products, respectively. Thereby, these processes, connected in the cell in series, are capacitive in nature and possess a characteristic timescale and frequency, by which they can be analytically separated, for example, via EIS [44]. At very high excitation frequencies, the capacitive elements in the electrochemical and mass transport processes act as short circuits and the measured impedance is equal to the HFR of the cell [36-38].

3.4.3 | Significance of OER and HER in AEMWE

In contrast to the highly acidic environment encountered in PEMWE, where the HER is considered to be a much faster process than the OER [36], in the alkaline reaction conditions in AWE and AEMWE, both OER and HER kinetics can significantly impact overall cell performance [38, 45–47]. In a recently published study, Ranz et al. employed distribution of relaxation time (DRT) analysis to deconvolute the EIS of a baseline AEMWE cell, similar to the cells tested in the present study [38]. A reference electrode was used to separate impedance signals of the half-cells and both the HER and OER were found to significantly impact overall cell resistance, with the HER apex appearing at 20–500 Hz and the OER apex appearing at 0.5–100 Hz. Similar characteristic frequencies are expected in the present study.

3.4.4 | Characteristic Time Scale of Mass Transport Phenomena in Water Electrolysis

It is sometimes stated that gas/liquid distribution and concentration gradients in a PEMWE or AEMWE react slowly to changes in current density. Thus, mass transport limitations are assumed to manifest in EIS with low peak frequencies of 0.1-1 Hz in the form of an additional resistive-capacitive impedance response, that is, an additional semi-circle. More specifically, MTLs are typically modelled simply with an additional non-ideal RC element [48, 49] or a finite-length Warburg element [50]. Further, it is commonly stated that mass transport limitations only take effect when a certain gas evolution rate is exceeded and that the magnitude of mass transport limitation is thereafter increasing with rising current density in an accelerating fashion. However, experimental studies using single electrodes have demonstrated that in any gas evolving electrochemical reaction, at any operation point, mass transport phenomena effect cell performance, not just limited to high current density operation [51]. In fact, Tafel slopes, measured at very low current densities, are often skewed by mass transport processes [52, 53]. Additionally, considering

that gas bubbles evolving on submerged electrodes are often very small and undergo nucleation, growth and detachment in quick succession, there seems to be no reason to assume that all mass transport limitations react to changes in current density slowly. Depending on many co-related factors, such as gas evolution rate, number and position of nucleation sites, electrode structure, forced convection, electrode wettability, gas bubbles may detach within several microseconds, milliseconds or seconds, whereas concentration gradients might react just as quickly. Moreover, not a single characteristic timescale, but a range of timescales is expected, as mass transport processes occur at many physically different points on an electrode. Accepting this more complex view of mass transport limitations in gas evolving electrodes, we suggest that mass transport limitations impact the impedance response of a water electrolysis cell in several different ways, and the emergence of an additional semi-circle at low frequencies when exceeding a certain current density threshold is possible but not required. In fact, the time delay between the modulation of the reaction rate and the changes in mass transport effects, such as concentration overpotential or bubble coverage, likely determines at what frequency range impedance is affected. If the reaction time of a mass transport effect is much shorter than the characteristic time constant of the gas generating reaction, the MTL will be registered as an increase in charge transfer resistance. If the reaction time is much larger, then a separate process should be found at lower frequencies than the reaction itself, that is, the commonly encountered MTL semi-circle.

3.5 | Single Cell Characterization Results

Figures 9 and 10 show the results of the electrochemical characterization of AEMWE single cells employing the reference SoA NF-MPL and APS-MPL as stand-alone PTEs and as CSs, respectively. Low-loading CLs were used in the latter case, with 0.1 $mg_{Pt}\ cm^{-2}$ and 0.4 $mg_{Ni/Fe\text{-}LDH}\ cm^{-2}$ directly deposited via spray-coating on cathode and anode MPLs, respectively. All measurements were carried out at 70°C, feeding 1 M KOH to both anode and cathode via natural convection. A 100 μm DURAION AEM, manufactured by Evonik, was used for all tests. Figure 8 presents all six cell configurations tested.

3.6 | APS-MPL and SoA NF-MPL as Stand-Alone PTEs

Figure 9 shows characterization results of the AEMEL single cells employing the APS-MPL and NF-MPL as stand-alone PTEs, without any additional CL, directly contacting the AEM. As such, the APS-MPL vastly improves electrolysis efficiency by lowering cell potential at 1 A cm⁻² by 172 and 298 mV, when installed as anode and cathode PTE, respectively, clearly demonstrating the superiority of the APS-MPL as PTE compared to the NF-MPL. The Nyquist plots of the EIS show no significant differences in HFR between the different cell configurations, suggesting that the stark cell performance enhancement is caused solely by changes in kinetic and/or mass transport behaviour. Further, this points out that the mm-PTL/NF-MPL interface likely does not contribute to the HFR in a significant manner, as the absence of this interface in the mm-PTL/APS-MPL single component does not show an ohmic effect. Because Ni is the catalytically active material in both

MPLs tested, shown via EDX and XRD analysis, the differences in electrochemical behaviour are plausibly solely a function of two aspects of the MPL structure:

- The internal surface area of the MPL and effective distance of the active surface to the AEM.
- 2. The distribution of conductive electrolyte, including water as reactant in the HER, as well as gaseous and dissolved reaction products inside the MPL at any operation point, impeding the reaction, controlled by the mass transport properties of the MPL, themselves being a complex function of many structural and surface parameters of the MPL, the nature of the surrounding liquid and evolving gases and the operating conditions.

3.6.1 | Onset Region

In the PTE setting, a significant reduction of onset potential of approximately 60 mV is achieved by switching from the NF-MPL to the APS-MPL on the anode. Beyond significant doubt, this is caused directly by the considerably higher internal surface area of the APS-MPL compared to the NF-MPL. The same MPL change on the cathode also leads to an onset potential reduction, although cell potential is higher than expected, leading to a reduced HFR-free $E(\log i)$ slope of the cell below 1.5 V. Such an effect is sometimes encountered in single electrode HER measurements and can be caused by the reoxidation of hydrogen at low negative HER potentials [53, 54]. In the experiments carried out here, this effect is only seen when the APS-MPL is used on the cathode and not registered when the NF-MPL is used on the cathode instead. This indicates that some of the internal area of the APS-MPL is covered with hydrogen gas, even at the lowest current densities.

3.6.2 | Intermediate Current Density Region

At intermediate current densities, between 0.02 and 0.05 A cm⁻², where the impact of the hydrogen oxidation reaction (HOR) seems to have largely disappeared, the HFR-free $E(\log i)$ slope is approximately constant and slightly reduced in the cells using the APS-MPL as stand-alone anode or cathode PTE at \sim 200 mV dec⁻¹ compared to the Ni felt MPL at \sim 230 mV dec⁻¹. Although close to the margin of error, at this current range, the effect of rising mass transport limitations caused by increasing bubble coverage or concentration overpotentials might already be impacting the cell performance, leading to an increase in HFRfree cell resistance that is correlated to the increase of HFR-free $E(\log i)$ slope. Figure S12A shows the HFR-free $E(\log i)$ slope of the PTE cells, showing an area of approximately constant region below 50 mA cm⁻² and following an accelerating increase. Similar behaviour was predicted by Vogt et al., who investigated the relationship between bubble surface coverage θ and current density, and found that θ is proportional to $i^{0.3}$ for flat electrodes in stagnant electrolyte, which does result in an accelerating increase of the HFR-free $E(\log i)$ slope due to the continuously increasing amount of inaccessible surface area [55]. This corroborates the assumption that the changes in HFR-free $E(\log i)$ slope observed are connected to mass transport limitations, more specifically

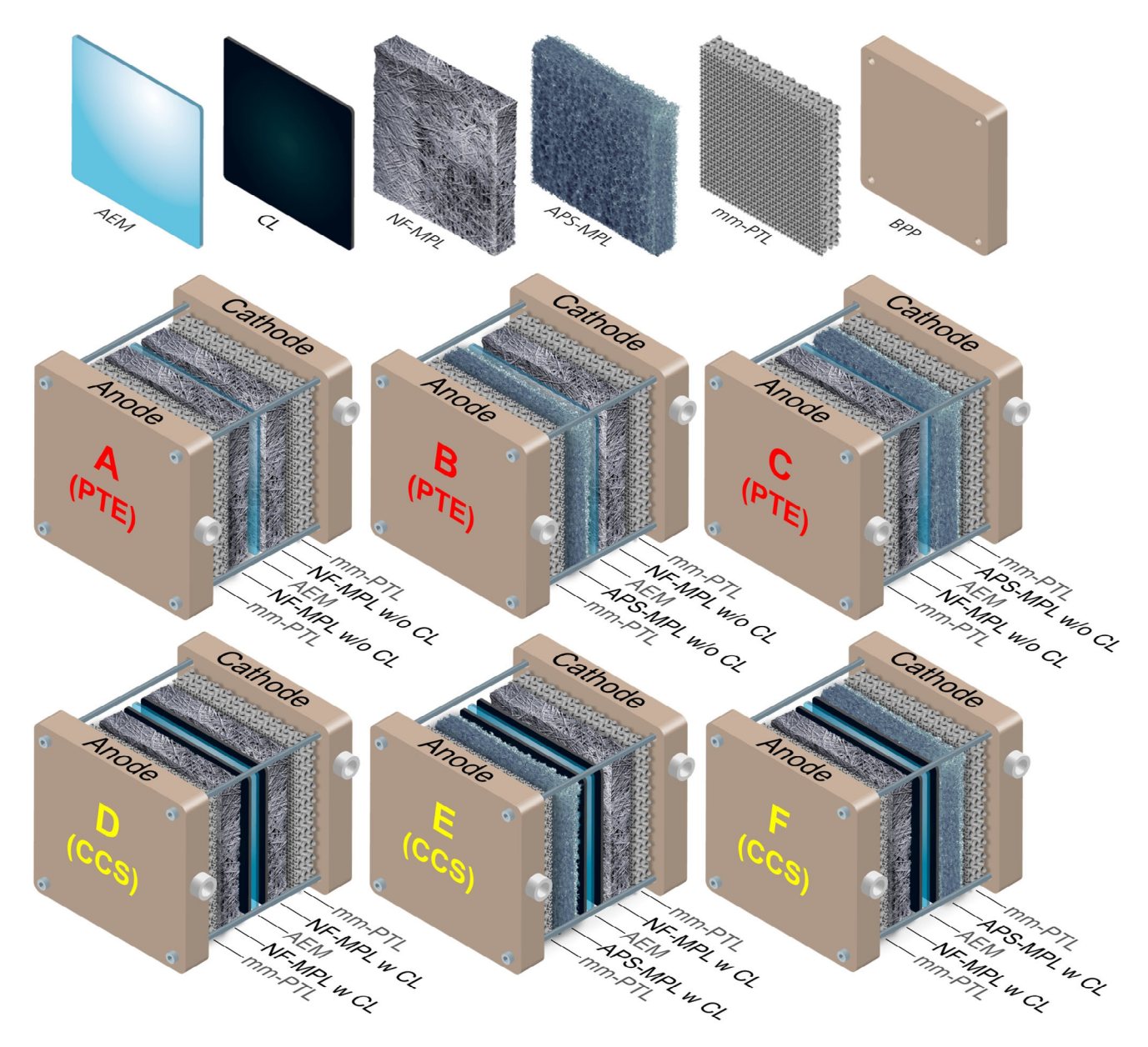


FIGURE 8 | Cell configuration of six AEMWE cells tested in this study. (A) Anode NF-MPL/Cathode NF-MPL, (B) anode APS-MPL/cathode NF-MPL, (C) anode NF-MPL/cathode APS-MPL, (D) anode NF-MPL + Ni/Fe-LDH/cathode NF-MPL + PtC, (E) anode APS-MPL + Ni/Fe-LDH/cathode APS-MPL + PtC, (F) anode NF-MPL + Ni/Fe-LDH/cathode APS-MPL + PtC. APS-MPL, atmospherically plasma sprayed micro porous layer; NF-MPL, nickel felt micro porous layer.

to the changed rate of bubble coverage increase as a function of geometric current density among the tested MPLs. The exact relationship of bubble coverage and current density will certainly diverge from the predictions made for flat electrodes, as in the present case 3D PTEs with complex internal structure were tested. Another effect that might plausibly contribute to the increase of the HFR-free $E(\log i)$ slope at higher current densities is the increasing resistance of the CL itself, which is a function of current density and is separate from the HFR [56]. In the present case, the distribution of conductive liquid electrolyte is itself principally affected by gas accumulation, which results in a complex coupling of CL resistance and bubble coverage, rendering the separation of mass transport resistance and CL resistance impossible. Finally, the change of the rate determining step (RDS) of the anode and cathode reactions can result in

a change of HFR-free $E(\log i)$ slope. However, such change is characterized by the transition from one regime of constant HFR-free $E(\log i)$ slope to another regime of constant HFR-free $E(\log i)$ slope [57, 58]. This was not observed in this study, as HFR-free $E(\log i)$ slope keeps increasing in all cases. It is thus deemed unlikely that a change in RDS is responsible for the observed increase in slope and equivalent cell resistance. In fact, this increase seems to be caused by increasing mass transport limitations and/or CL resistance, both being affected by increasing bubble coverage.

The switch from NF-MPL to APS-MPL is reflected in the EIS recorded at 0.1 A cm⁻² by the reduction of the resistance of a high peak frequency resistive–capacitive process at approximately 100 Hz and a low peak frequency resistive–capacitive process at

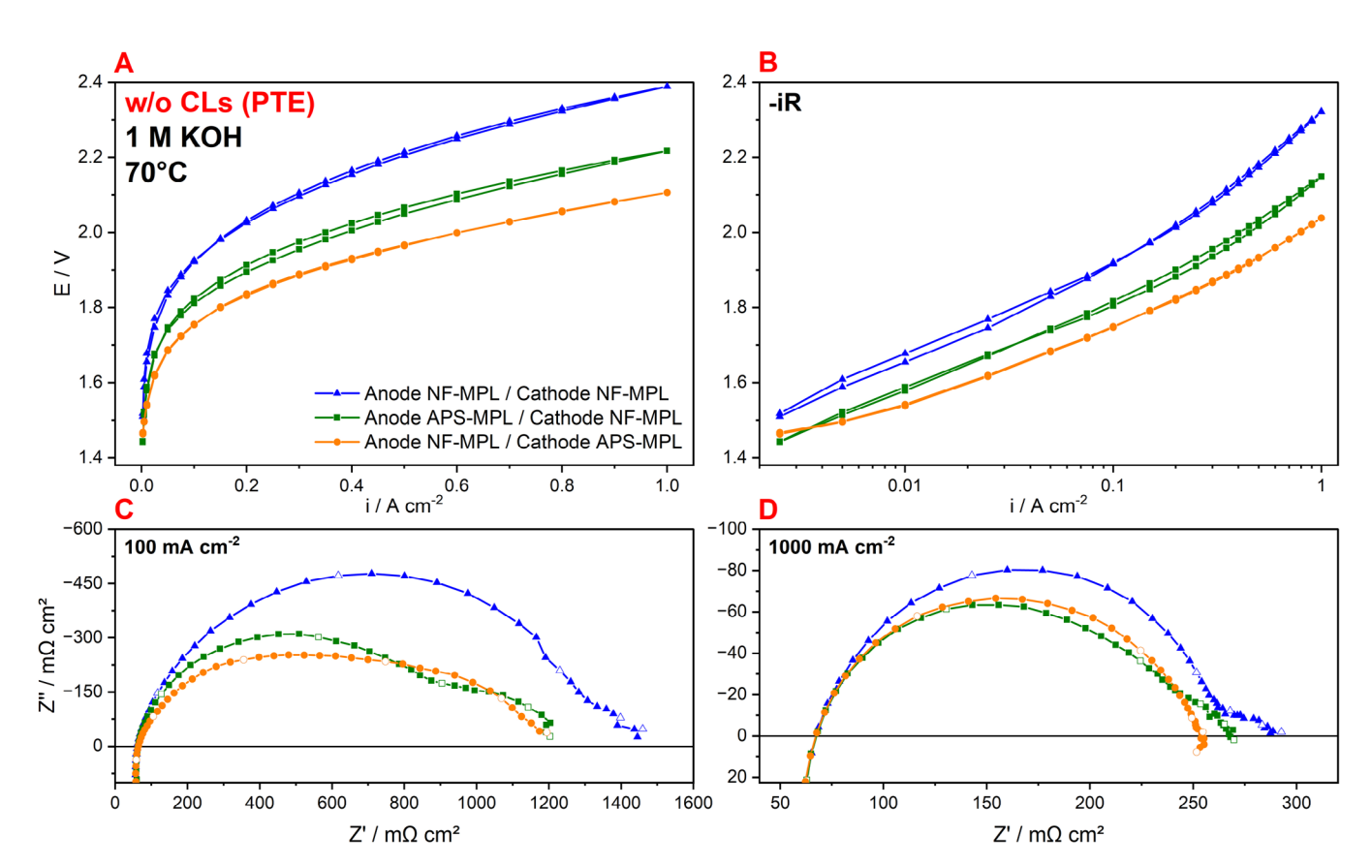


FIGURE 9 Characterization results of AEMWE single cells using the NF-MPL or APS-MPL as PTE without additional catalyst, measured at 70°C, feeding 1 M KOH to both anode and cathode, (A) *IV*-curve up to 1 A cm⁻², (B) HFR-free *IV*-curve, logarithmic abscissa, (C) Nyquist plot of EIS recorded at 100 mA cm⁻², (D) Nyquist plot of EIS recorded at 1000 mA cm⁻². Open symbols in Nyquist plots at approximately 10,000, 1000, 100, 10, 1 and 0.1 Hz. APS-MPL, atmospherically plasma sprayed micro porous layer; NF-MPL, nickel felt micro porous layer; PTE, porous transport electrode.

approximately 25 Hz, on cathode and anode, respectively. This direct correlation, together with results of a previous study [38], constitutes strong evidence that high and low frequency processes found in the EIS are directly linked to the charge transfer during HER and OER, respectively. The EIS recorded of the cell utilizing an NF-MPL as both anode and cathode shows strong overlapping of the OER and HER process, seemingly resulting in a single EIS feature. Analogous to the reduction in HFR-free $E(\log i)$ slope, the reduction in apparent charge transfer resistances can be assigned to the reduced rate of bubble coverage increase as a function of geometric current density using the APS-MPL instead of the NF-MPL.

3.6.3 | High Current Density Region

At high current densities above 100 mA cm $^{-2}$ HFR-free $E(\log i)$ slopes of all cells using the MPLs as stand-alone PTEs increase in an accelerating fashion, presumably as evolving gas bubbles begin to block the active electrode surfaces and displace conductive electrolyte to a more and more significant degree. The slope eventually reached at 1 A cm $^{-2}$ is lowest in the cathode APS-MPL cell at 370 mV dec $^{-1}$. In comparison, the final slope at 1 A cm $^{-2}$ is 500 mV dec $^{-1}$ for the cell using the APS-MPL only on the anode and 540 mV dec $^{-1}$ for the cell using the NF-MPL as both stand-alone PTEs. The EIS recorded at 1 A cm $^{-2}$ reveal that the emergence of a low frequency resistive–capacitive process (peak

frequency \sim 5 Hz) is prevented by employing the APS-MPL as cathode PTE. This process can be assigned to gas accumulation taking place on a longer time scale, which seems to be occurring on the low surface area NF-MPL but is not encountered on the high surface area APS-MPL. However, the resistance contribution of the resistive-capacitive process at 5 Hz does only account for a small part of the HFR-free $E(\log i)$ slope difference.

More significant, as was the case in the low current density region, is the direct reduction of the apparent resistance of the respective charge transfer processes of anode and cathode at higher peak frequencies. This is in line with the proposition stated earlier that bubble coverage and concentration gradients could change effectively in unison with reaction rate. The reduction of the HFR-free $E(\log i)$ slope and total cell impedance eventually reached at 1 A cm⁻² using the APS-MPL as cathode PTE, compared to the NF-MPL, is moreover likely connected to the significantly reduced rate of bubble coverage increase as a function of current density. The stark difference in behaviour between the magnitude of the effect of the APS-MPL on anode and cathode might plausibly be caused by differences in kinetics and resistance contributions to overall cell resistance of HER and OER. However, another explanation is the existence of a fundamental difference in gas bubble behaviour in the PTEs between anode and cathode, due to which evolving oxygen leads to more severe bubble coverage and a faster increase in bubble coverage in the APS-MPL structure as a function of current

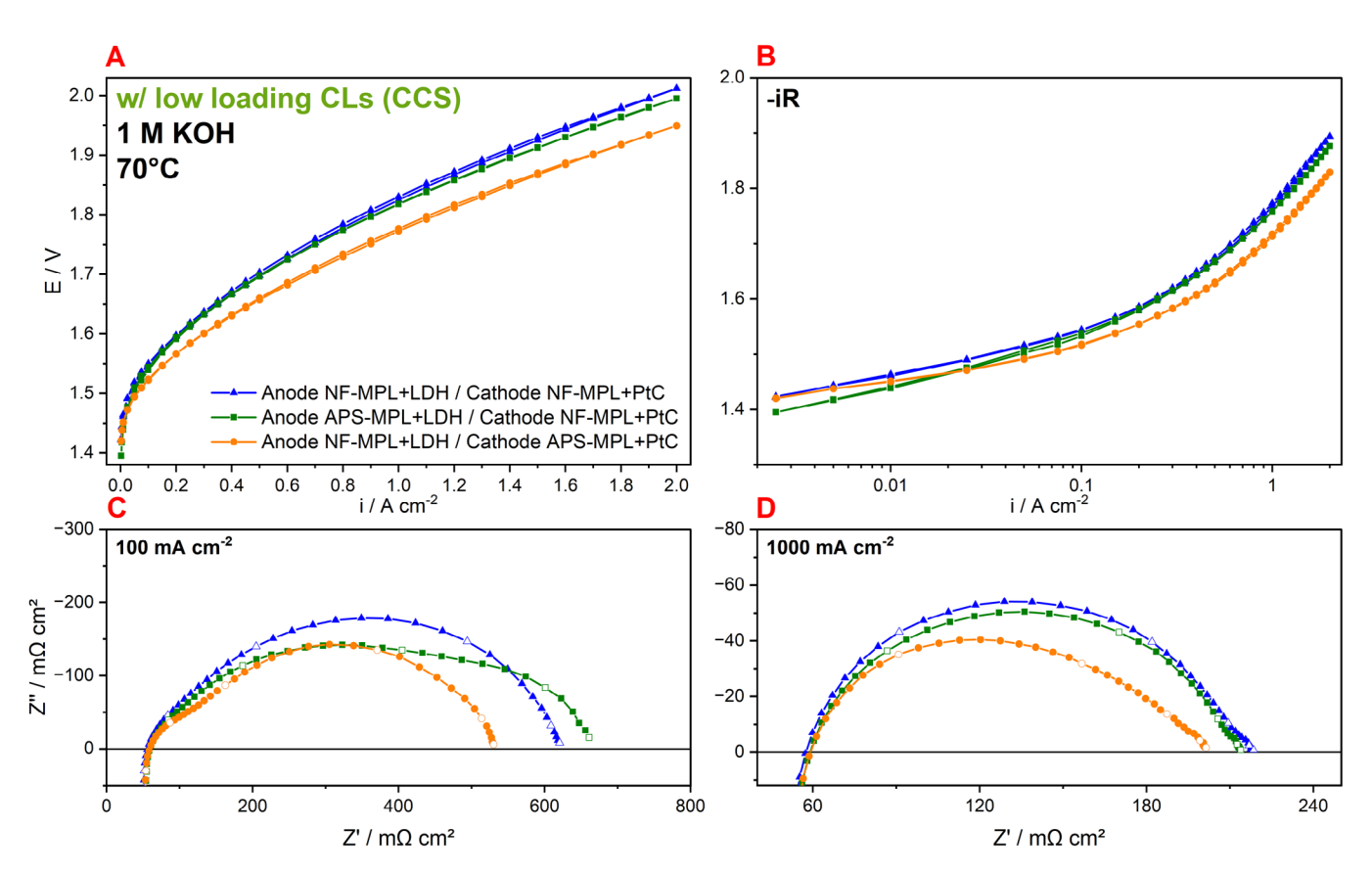


FIGURE 10 | Characterization results of AEMWE single cells using the NF-MPL or APS-MPL as CCS with low loading CLs, measured at 70°C, feeding 1 M KOH to both anode and cathode, (A) IV-curve up to 1 A cm⁻², (B) HFR-free IV-curve, logarithmic abscissa, (C) Nyquist plot of EIS recorded at 100 mA cm⁻², (D) Nyquist plot of EIS recorded at 1000 mA cm⁻². Open symbols in Nyquist plots at approximately 10,000, 100, 10, 1 and 0.1 Hz. APS-MPL, atmospherically plasma sprayed-micro porous layer; CCS, catalyst-coated substrate; CLs, catalyst layers; NF-MPL, nickel felt micro porous layer; PTE, porous transport electrode.

density than evolving hydrogen. The results of a recent study by Kitajima et al. provide some supporting evidence, as the authors found that gas bubble coverage had a more severe impact in the OER compared to the HER on an Ni wire electrode in 2 M KOH, due to the much larger oxygen bubble diameter, compared to the hydrogen bubble diameter [43]. It was further noted by Chin et al. that oxygen bubbles show a higher tendency to coalesce than hydrogen bubbles [59]. It is therefore reasonable to assume that the ideal cathode MPL and ideal anode MPL for an AEMWE might differ significantly in their structural parameters and that this should be kept in mind during the development of such components.

3.6.4 | Tests With APS-MPL as Anode and Cathode

Figure S13 shows all electrochemical characterization results recorded in the PTE setting, including data recorded of a cell employing the APS-MPL as both anode and cathode electrode. At low potentials, a 10-fold current density increase compared to the full NF-MPL cell was measured, approximately corresponding to a 10-fold increase in available and electrochemically active surface area at 1.5 V cell potential. At higher current densities the APS-MPL|AEM|APS-MPL cell behaves unexpectedly, as the HFR-free $E(\log i)$ slope and total cell impedance increases more significantly compared to the other cells tested in a PTE setting.

After disassembly, it was found that over a large part of the MEA, proper connection between PTE and AEM was not established, forming a gap between electrode and AEM, where gases can accumulate (Figure S14). This change is reflected in an overall deformation of the EIS curves and an increase of imaginary impedance at low frequencies. We hypothesize that gas accumulation in the PTE|AEM gap is responsible for the changes in characteristics, as it might increase effective CL resistance due to the displacement of the conductive electrolyte phase and increase mass transport limitations. The improper contact was caused by a slight bend in both APS-MPLs. This bend was inconsequential for the previous tests, as the soft NF-MPL was able to conform to the oppositely placed APS-MPL. This interesting observation shows that achieving flatness is extremely important when using rigid PTL/MPLs.

3.7 | APS-MPL and SoA NF-MPL as Catalyst Substrates (CSs)

Figure 10 shows analogous characterization results, but instead testing the MPLs in combination with low-loading CLs, directly deposited on the MPLs via spray coating, generating CCS-style electrodes. The use of the APS-MPL as anode and cathode CS reduces cell potential at 2 A cm⁻² by 17 and 63 mV, respectively, compared to the SoA Ni felt MPL. As a key take-away of this study,

this shows that APS can be used to create CSs that outperform SoA materials, at reduced manufacturing costs. As was the case in tests without CLs, the HFR is not impacted by MPL type. Nyquist plots of the EIS of cells with CLs once more show a high frequency resistive-capacitive process, likely linked to the cathode HER process and a low frequency resistive-capacitive process, likely linked to the anode OER. With the addition of the CLs, we propose that the cell performance is impacted by four main aspects connected to MPL presence:

- The activity of the accessible internal surface of the MPL, contributing to the overall electrode performance, itself being a function of internal surface area and correlated mass transport management.
- The efficiency of the mass transport of liquid electrolyte and reactant into the CL and of dissolved or gaseous products out of the CL, determined by surface and structural parameters of the MPL, likely impacted by gas evolution within the MPL.
- 3. The morphology of the CL, determining the amount of physically blocked catalyst or ionically ill connected catalyst as well as the mass transport within the CL and quality of the electrical connection between MPL and CL.
- 4. The uniformity of the compression of the CL, as this can improve percolation and electrical connection between catalyst particles [31, 60].

3.7.1 | Onset Region

As was laid out discussing the PTE test results, the increased cell potential and reduced HFR-free $E(\log i)$ slope below 1.5 V of the cell employing the APS-MPL as CS on the cathode can be explained by high hydrogen retention inside the APS-MPL leading to significant HOR current. We hypothesize that the visible high-frequency deformation of the spectrum recorded at 0.1 A cm $^{-2}$ with a peak frequency of approximately 1000 Hz of the cell operating with an APS-MPL CS might be connected to the occurring HOR.

As was found in the PTE setting, onset potential is reduced by the use of the APS-MPL instead of the NF-MPL as CS on the anode, indicating a significant increase of active surface. This effect is also expected on the cathode but is masked by the proposed cell potential increasing HOR effect. To differentiate between an increase in active surface solely due to the increased active surface of the Ni MPL and an increase of active surface due to improved CL utilization, results of the PTE and CCS tests are compared. At a cell potential of 1.5 V, switching from the NF-MPL to the APS-MPL on the anode leads to a current density increase of approximately 2.5 mA cm⁻² in the PTE setting, and approximately 15 mA cm⁻² in the CCS setting. On the cathode the same modification leads to a current density increase of approximately 5 mA cm⁻² at 1.5 V in the PTE setting, and approximately 30 mA cm⁻² in the CCS setting. For both electrodes, this increase is approximately six times higher in the CCS setting compared to the PTE setting, indicating that the APS-MPL, when used as anode or cathode CS leads to a significant increase in catalyst utilization at low current densities, as the vast majority of the performance increase cannot be attributed to the more active MPL. The superiority of the APS-MPL compared to the NF-MPL as CS at low current densities is likely due to the improved CL morphology. The low-density NF-MPL contains many large pores that penetrate the complete structure or part of the structure, leading to a reduced projection area and higher average distance between MPL and AEM, respectively. At equal catalyst loading, the CL thickness and average distance between CL and AEM is thus larger on the NF-MPL, compared to the APS-MPL, which does not contain any large, straight and deeply penetrating pores. The reduction in CL thickness likely reduces ohmic drop and mass transport limitations within the CL, both reducing overpotential in the CL, with the latter being due to reduced accumulation of reaction products. Additionally, caused by the larger and deeper pores on the NF-MPL surface, it is probable that some of the CL is not properly compressed as it is not in contact with the AEM. This portion of the CL is likely less active, as CL percolation by compression has been shown to be essential to establish sufficient CL conductivity [31, 60]. Furthermore, it is reasonable to assume that during the spray coating process, small pores on the surface of the APS-MPL are penetrated by the ink via capillary forces, leading to intrusion of the CL into the APS-MPL, further reducing average CL thickness and improving the CL|MPL interface. Although no durability tests were carried out in this study, significantly less CL transfer to the AEM was registered using the APS-MPL as CS, compared to the NF-APS, showing the improved MPL-CL connection caused by the high rugosity APS-MPL surface (Figure S15).

3.7.2 | Intermediate Current Density Region

Qualitatively, the relationship of HFR-free $E(\log i)$ slope and current density is similar to the PTE scenario, although differences between MPL-type are less significant. Unlike when used as stand-alone anode PTE, as anode CS, the APS-MPL leads to increased HFR-free $E(\log i)$ slope at low current densities below 0.1 A cm⁻² (92 mV dec⁻¹), compared to the Ni felt MPL (80 mV dec⁻¹), connected to an increase of the resistance of the low-frequency resistive–capacitive OER process in the EIS. As it is unlikely that the change in catalyst morphology itself (thinner CL, higher interface area, improved percolation) induces an increase of HFR-free $E(\log i)$ slope of the OER, this is likely connected to increased mass transport limitations within the MPL, adjacent to the anode CL.

The supposed effect of the HOR strongly impacts the HFR-free $E(\log i)$ slope of the cathode APS-MPL-CS cell. Nevertheless, the shape and position of the polarization curve at higher current densities suggests that in the absence of the HOR phenomenon, HFR-free $E(\log i)$ slope at low current densities might be similar to the NF-MPL as CS, suggesting that the APS-MPL does not negatively impact mass transport efficiency on the cathode at low current densities, as it seems to do on the anode.

3.7.3 | High Current Density Region

At high current densities, compared to the Ni felt CS (380 mV dec⁻¹ at 1 A cm⁻²), the APS-MPL-CS leads to reduced

HFR-free $E(\log i)$ slope at anode (350 mV dec⁻¹ at 1 A cm⁻²) and cathode (330 mV dec⁻¹). This is reflected in the EIS by the reduction of the high-frequency process when the APS-MPL-CS is put on the cathode, whereas the change in the anode is less clearly visible, due to its smaller magnitude. Similar to the PTE-test results, the CCS results suggest that the novel APS-MPL facilitates mass transport on the cathode, while having a reduced impact on the anode.

3.7.4 | Summary of Test Results

In summary, using the APS-MPL as stand-alone PTE on anode or cathode leads to onset potential reduction and a shift of the polarization curves to higher current densities. This is directly caused by the higher accessible electrochemically active surface area. However, it should be noted that the observed 10-fold increased current density at low potentials in tests with the APS-MPL as both anode and cathode PTE is not proportional to the measured 60-fold SSA increase achieved by switching from NF-MPL to APS-MPL. This suggests that a large part of the APS-MPL is gas filled starting at low current density conditions and is not taking part in the reaction. Especially the high tortuosity secondary pore structure within the primary nickel skeleton is likely not provided with sufficient water and electrolyte during operation. The presumed strong impact of the HOR at low potentials connected to high gas retention corroborates this assumption. In general, this observation is in line with results from literature. For example, Rocha et al. [61] reported that a reduction of the pore size of an Ni foam electrode from 3000 to 800 µm caused a very significant increase in relative bubble coverage of the internal surface of the electrode at constant SSA normalized current density. Nevertheless, in the present study, HFR-free $E(\log i)$ slopes, directly connected to the rate of bubble coverage increase as a function of geometric current density, are reduced throughout the operation window using the APS-MPL, more significantly at high current densities and most significantly at high current densities while using the APS-MPL as cathode stand-alone PTE. These findings indicate that although a significant part of the internal surface of the APS-MPL is blocked by gas throughout the operation window, the remaining accessible surface, which appears to be approximately 10 times larger than the accessible surface on the NF-MPL, on the basis of the electrochemical characterization results, can facilitate mass transport efficiently. This might be simply due to the reduced surface specific gas evolution rate reducing the increase of bubble coverage but could be additionally facilitated by other structural properties of the MPL. Differentiation between the effect of mass transport impacting structural properties (pore size, tortuosity, wettability and multi-modality of the PSD) and the effect of higher available electrochemically accessible surface area on the rate of bubble coverage increase is difficult. Thus, for the evaluation of the efficacy of such structural properties, MPLs with similar total SSA should be compared.

In a CCS configuration, analysis of the cell behaviour at low current densities shows that the APS-MPL increases catalyst utilization significantly, that is, increases current density, corrected to not include the inherent activity of the MPL, at a fixed cell potential, compared to the NF-MPL. This is likely due to the flatter and thinner CL on the APS-MPL surface, reducing catalyst blockage and mass transport limitations within the CL and increasing percolation and thereby conductivity of the CL. At high current densities HFR-free E(log i) slope and total cell impedance in EIS measurements are reduced when using the APS-MPL as CS on anode or cathode, demonstrating the superior ability to remove gas from the CL and provide reactant and electrolyte to the CL, facilitated by the improved structural properties of the APS-MPL compared to the NF-MPL. However, it is not possible to differentiate between effects caused by CL morphology and internal MPL structure. Beyond increasing initial performance, it was found that the high rugosity APS-MPL improved the CL/MPL connection compared to the NF-MPL. Remarkably, at low current densities, employing the APS-MPL as CS on the anode leads to an increase of the HFRfree $E(\log i)$ slope, whereas the opposite is the case when using the APS-MPL as CS on the cathode. This suggests a difference in bubble behaviour between hydrogen and oxygen within the MPL.

4 | Conclusion

Apart from the availability of low-cost green electricity, electrolyser investment cost, to which the PTL/MPL component contributes significantly, is holding back the commercialization of AEMWE. In this study, we replaced an expensive SoA Ni felt MPL with a novel, easily upscaled MPL, generated by directly depositing an Ni/C layer on a mesh PTL via APS and subsequent oxidative removal of the carbon to induce high porosity of up to 45%. As cathode CS this MPL increased AEMWE performance by lowering cell potential by 63 mV at 2 A cm⁻² compared to an SoA NF-MPL. The developed APS-MPL was further characterized as stand-alone PTE, confirming that the performance increase measured when used as CS goes beyond the increase in MPL activity and to a large degree is likely due to enhanced catalyst utilization. The increase in catalyst utilization is believed to be caused by the improved CL morphology and/or more efficient transport of liquid and gas through the novel APS-MPL. MIP and FIB-SEM analysis revealed that the novel APS-MPL exhibits a bi-modal porous structure with a high internal surface area, including a primary structure with 1-10 µm diameter pores and a secondary structure with 0.01-1 µm diameter pores. The broad pore size distribution of the APS-MPL might facilitate the formation of preferential pathways for liquid and gas transport, alleviating mass transport limitations compared to an SoA NF-MPL. Additionally, the high rugosity surface area of the APS-MPL led to improved CL adhesion shown by reduced CL transferral to the AEM, indicating that the novel APS-MPL can improve AEMWE durability. In future work on the APS-MPL approach, the aspect of CL-stabilization will be investigated in long-term durability tests. Further optimization of structural properties of the APS-MPL, such as reducing tortuosity by increasing the pore-size of the primary pore network, while maintaining high SSA and surface rugosity, could additionally improve this concept. Besides, the use of a pore-forming agent that can be removed from the APS layer more easily, with reduced time and energy demand, will improve the economic attractiveness of the approach.

Acknowledgements

This work was carried out within the project AEM-Direkt (Förderkennzeichen 03HY130) funded by the German Ministry of Science and Education (BMBF).

Open access funding enabled and organized by Projekt DEAL.

Conflicts of Interest

The authors declare no conflicts of interest.

Data Availability Statement

The data that support the findings of this study are available from the corresponding author upon reasonable request.

References

- 1. O. Schmidt, S. Melchior, A. Hawkes, and I. Staffell, "Projecting the Future Levelized Cost of Electricity Storage Technologies," *Joule* 3, no. 1 (2019): 81–100.
- 2. N. Rambhujun, M. S. Salman, T. Wang, et al., "Renewable Hydrogen for the Chemical Industry," *MRS Energy Sustain* 7, no. 1 (2020): 33.
- 3. E. Jacobasch, G. Herz, C. Rix, et al., "Economic Evaluation of Low-Carbon Steelmaking via Coupling of Electrolysis and Direct Reduction," *Journal of Cleaner Production* 328 (2021): 129502.
- 4. P. D. Cavaliere, A. Perrone, and A. Silvello, "Water Electrolysis for the Production of Hydrogen to Be Employed in the Ironmaking and Steelmaking Industry," *Metals* 11, no. 11 (2021): 1816.
- 5. H. Nami, P. V. Hendriksen, and H. L. Frandsen, "Green Ammonia Production Using Current and Emerging Electrolysis Technologies," *Renewable and Sustainable Energy Reviews* 199 (2024): 114517.
- 6. L. Colelli, V. Segneri, C. Bassano, and G. Vilardi, "E-Fuels, Technical and Economic Analysis of the Production of Synthetic Kerosene Precursor as Sustainable Aviation Fuel," *Energy Conversion and Management* 288 (2023): 117165.
- 7. Y. Leng, G. Chen, A. J. Mendoza, T. B. Tighe, M. A. Hickner, and C.-Y. Wang, "Solid-State Water Electrolysis With an Alkaline Membrane," *Journal of the American Chemical Society* 134, no. 22 (2012): 9054–9057.
- 8. N. Du, C. Roy, R. Peach, M. Turnbull, S. Thiele, and C. Bock, "Anion-Exchange Membrane Water Electrolyzers," *Chemical Reviews* 122, no. 13 (2022): 11830–11895.
- 9. C. Li and J.-B. Baek, "The Promise of Hydrogen Production From Alkaline Anion Exchange Membrane Electrolyzers," *Nano Energy* 87 (2021): 106162.
- 10. H. A. Miller, K. Bouzek, J. Hnat, et al., "Green Hydrogen From Anion Exchange Membrane Water Electrolysis: A Review of Recent Developments in Critical Materials and Operating Conditions," *Sustainable Energy & Fuels* 4, no. 5 (2020): 2114–2133.
- 11. F. Li, S. H. Chan, and Z. Tu, "Recent Development of Anion Exchange Membrane Fuel Cells and Performance Optimization Strategies: A Review," *Chemical Record* 24, no. 1 (2024): e202300067.
- 12. Energy Transitions Commission (ETC), Making the Hydrogen Economy Possible: Making the Hydrogen Economy Possible (London: Energy Transitions Commission (ETC), 2021).
- 13. International Renewable Energy Agency (IRENA), *Green Hydrogen Cost Reduction: Scaling up Electrolysers to Meet the 1.5* ^o *C Climate Goal* (Masdar: International Renewable Energy Agency (IRENA), 2020).
- 14. M. Kim, D. Lee, M. Qi, and J. Kim, "Techno-Economic Analysis of Anion Exchange Membrane Electrolysis Process for Green Hydrogen Production Under Uncertainty," *Energy Conversion and Management* 302 (2024): 118134.

- 15. J. E. Park, H. J. Choi, S. Y. Kang, et al., "Effect of Pore Structures in Nickel-Based Porous Transport Layers for High-Performance and Durable Anion-Exchange Membrane Water Electrolysis," *International Journal of Energy Research* 46, no. 12 (2022): 16670–16678.
- 16. F. Razmjooei, T. Morawietz, E. Taghizadeh, et al., "Increasing the Performance of an Anion-Exchange Membrane Electrolyzer Operating in Pure Water With a Nickel-Based Microporous Layer," *Joule* 5, no. 7 (2021): 1776–1799.
- 17. N. U. Hassan, E. Motyka, J. Kweder, et al., "Effect of Porous Transport Layer Properties on the Anode Electrode in Anion Exchange Membrane Electrolyzers," *Journal of Power Sources* 555 (2023): 232371.
- 18. Y. Tao, M. Wu, M. Hu, et al., "High-Performance Porous Transport Layers for Proton Exchange Membrane Water Electrolyzers," *SusMat* 4 (2024): e230.
- 19. Q. Xu, S. Z. Oener, G. Lindquist, H. Jiang, C. Li, and S. W. Boettcher, "Integrated Reference Electrodes in Anion-Exchange-Membrane Electrolyzers: Impact of Stainless-Steel Gas-Diffusion Layers and Internal Mechanical Pressure," *ACS Energy Letters* 6, no. 2 (2020): 305–312.
- 20. B. Huang, X. Wang, W. Li, et al., "Accelerating Gas Escape in Anion Exchange Membrane Water Electrolysis by Gas Diffusion Layers With Hierarchical Grid Gradients," *Angewandte Chemie (International ed in English)* 62, no. 33 (2023): e202304230.
- 21. P. Lettenmeier, S. Kolb, N. Sata, et al., "Comprehensive Investigation of Novel Pore-Graded Gas Diffusion Layers for High-Performance and Cost-Effective Proton Exchange Membrane Electrolyzers," *Energy & Environmental Science* 10, no. 12 (2017): 2521–2533.
- 22. L.i. Wang, T. Weissbach, R. Reissner, et al., "High Performance Anion Exchange Membrane Electrolysis Using Plasma-Sprayed, Non-Precious-Metal Electrodes," *ACS Applied Energy Materials* 2, no. 11 (2019): 7903–7912.
- 23. S. Stiber, N. Sata, T. Morawietz, et al., "A High-Performance, Durable and Low-Cost Proton Exchange Membrane Electrolyser With Stainless Steel Components," *Energy & Environmental Science* 15, no. 1 (2022): 109–122.
- 24. A. Kiessling, J. C. Fornaciari, G. Anderson, et al., "Influence of Supporting Electrolyte on Hydroxide Exchange Membrane Water Electrolysis Performance: Anolyte," *Journal of The Electrochemical Society* 168, no. 8 (2021): 084512.
- 25. A. Kiessling, J. C. Fornaciari, G. Anderson, et al., "Influence of Supporting Electrolyte on Hydroxide Exchange Membrane Water Electrolysis Performance: Catholyte," *Journal of The Electrochemical Society* 169, no. 2 (2022): 024510.
- 26. S. Shaik, J. Kundu, Y. Yuan, et al., "Recent Progress and Perspective in Pure Water-Fed Anion Exchange Membrane Water Electrolyzers," *Advanced Energy Materials* 14 (2024): 2401956.
- 27. F. Razmjooei, R. Reißner, A. S. Gago, and A. Ansar, "Highly Active Binder Free Plasma Sprayed NonNoble Metal Electrodes for Anion Exchange Membrane Electrolysis at Different Reduced KOH Concentrations," *ECS Transactions* 92 (2019): 689–702.
- 28. M. Klingenhof, P. Hauke, M. Kroschel, et al., "Anion-Tuned Layered Double Hydroxide Anodes for Anion Exchange Membrane Water Electrolyzers: From Catalyst Screening to Single-Cell Performance," *ACS Energy Letters* 7, no. 10 (2022): 3415–3422.
- 29. M. Klingenhof, P. Hauke, S. Brückner, et al., "Modular Design of Highly Active Unitized Reversible Fuel Cell Electrocatalysts," *ACS Energy Letters* 6, no. 1 (2020): 177–183.
- 30. T. Malkow, A. Pilenga, G. Tsotridis, and G. De Marco, *EU Harmonised Polarisation Curve Test Method for Low Temperature Water Electrolysis* (Brussels: European Commission, 2018).
- 31. T. Schuler, J. M. Ciccone, B. Krentscher, et al., "Hierarchically Structured Porous Transport Layers for Polymer Electrolyte Water Electrolysis," *Advanced Energy Materials* 10, no. 2 (2019): 1903216.

- 32. K. V. Manukyan, A. G. Avetisyan, C. E. Shuck, et al., "Nickel Oxide Reduction by Hydrogen: Kinetics and Structural Transformations," *Journal of Physical Chemistry C* 119, no. 28 (2015): 16131–16138.
- 33. T. Schuler, R. De Bruycker, T. J. Schmidt, and F. N. Büchi, "Polymer Electrolyte Water Electrolysis: Correlating Porous Transport Layer Structural Properties and Performance: Part I. Tomographic Analysis of Morphology and Topology," *Journal of The Electrochemical Society* 166, no. 4 (2019): F270–F281.
- 34. C. Xu, J. Wang, J. Wang, et al., "Structural Optimization Study on Porous Transport Layers of Sintered Titanium for Polymer Electrolyte Membrane Electrolyzers," *Applied Energy* 357 (2024): 122541.
- 35. T. Kadyk, D. Bruce, and M. Eikerling, "How to Enhance Gas Removal From Porous Electrodes?," *Scientific Reports* 6 (2016): 38780.
- 36. C. Rozain and P. Millet, "Electrochemical Characterization of Polymer Electrolyte Membrane Water Electrolysis Cells," *Electrochimica Acta* 131 (2014): 160–167.
- 37. X. Huo, G. Shan, L. Yang, et al., "Impedance Analysis of Alkaline Water Electrolysis Based on Distribution of Relaxation Time," *International Journal of Hydrogen Energy* 53 (2024): 684–697.
- 38. M. Ranz, B. Grabner, B. Schweighofer, H. Wegleiter, and A. Trattner, "Dynamics of Anion Exchange Membrane Electrolysis: Unravelling Loss Mechanisms With Electrochemical Impedance Spectroscopy, Reference Electrodes and Distribution of Relaxation Times," *Journal of Power Sources* 605 (2024): 234455.
- 39. H. Vogt and K. Stephan, "Local Microprocesses at Gas-Evolving Electrodes and Their Influence on Mass Transfer," *Electrochimica Acta* 155 (2015): 348–356.
- 40. H. Vogt, "The Concentration Overpotential of Gas Evolving Electrodes as a Multiple Problem of Mass Transfer," *Journal of The Electrochemical Society* 137 (1990): 1179.
- 41. M. Bernt and H. A. Gasteiger, "Influence of Ionomer Content in IrO2/TiO2Electrodes on PEM Water Electrolyzer Performance," *Journal of The Electrochemical Society* 163, no. 11 (2016): F3179–F3189.
- 42. H. Ikeda, R. Misumi, Y. Nishiki, Y. Kuroda, and S. Mitsushima, "A Dual Bubble Layer Model for Reactant Transfer Resistance in Alkaline Water Electrolysis," *Electrochimica Acta* 430 (2022): 141053.
- 43. D. Kitajima, R. Misumi, Y. Kuroda, and S. Mitsushima, "Relationship Between Bubble Generation Behavior and Hydrogen Evolution Reaction Performance at High Current Densities During Alkaline Water Electrolysis," *Electrochimica Acta* 502 (2024): 144772.
- 44. S. Wang, J. Zhang, O. Gharbi, V. Vivier, M. Gao, and M. E. Orazem, "Electrochemical Impedance Spectroscopy," *Nature Reviews Methods Primers* 1, no. 1 (2021): 41.
- 45. I. V. Pushkareva, M. A. Solovyev, S. I. Butrim, M. V. Kozlova, D. A. Simkin, and A. S. Pushkarev, "On the Operational Conditions' Effect on the Performance of an Anion Exchange Membrane Water Electrolyzer: Electrochemical Impedance Spectroscopy Study," *Membranes (Basel)* 13, no. 2 (2023): 192.
- 46. W. Sheng, H. A. Gasteiger, and Y. Shao-Horn, "Hydrogen Oxidation and Evolution Reaction Kinetics on Platinum: Acid vs Alkaline Electrolytes," *Journal of The Electrochemical Society* 157, no. 11 (2010): B1529–B1536.
- 47. A. Y. Faid, A. O. Barnett, F. Seland, and S. Sunde, "NiCu Mixed Metal Oxide Catalyst for Alkaline Hydrogen Evolution in Anion Exchange Membrane Water Electrolysis," *Electrochimica Acta* 371 (2021): 137871.
- 48. S. Stiber, H. Balzer, A. Wierhake, et al., "Porous Transport Layers for Proton Exchange Membrane Electrolysis under Extreme Conditions of Current Density, Temperature, and Pressure," *Advanced Energy Materials* 11, no. 33 (2021): 2100630.
- 49. S. H. Frensch, A. C. Olesen, S. S. Araya, and S. K. Kær, "Model-Supported Characterization of a PEM Water Electrolysis Cell for the Effect of Compression," *Electrochimica Acta* 263 (2018): 228–236.

- 50. J. C. Garcia-Navarro, M. Schulze, and K. A. Friedrich, "Measuring and Modeling Mass Transport Losses in Proton Exchange Membrane Water Electrolyzers Using Electrochemical Impedance Spectroscopy," *Journal of Power Sources* 431 (2019): 189–204.
- 51. X. Zhao, H. Ren, and L. Luo, "Gas Bubbles in Electrochemical Gas Evolution Reactions," *Langmuir* 35, no. 16 (2019): 5392–5408.
- 52. O. Van Der Heijden, S. Park, J. J. J. Eggebeen, and M. T. M. Koper, "Non-Kinetic Effects Convolute Activity and Tafel Analysis for the Alkaline Oxygen Evolution Reaction on NiFeOOH Electrocatalysts," *Angewandte Chemie (International ed in English)* 62, no. 7 (2023): e202216477.
- 53. C. Wan, Y. Ling, S. Wang, et al., "Unraveling and Resolving the Inconsistencies in Tafel Analysis for Hydrogen Evolution Reactions," *ACS Central Science* 10, no. 3 (2024): 658–665.
- 54. Q. Chen, L. Luo, and H. S. White, "Electrochemical Generation of a Hydrogen Bubble at a Recessed Platinum Nanopore Electrode," *Langmuir* 31, no.15 (2015): 4573–4581.
- 55. H. Vogt and R. J. Balzer, "The Bubble Coverage of Gas-Evolving Electrodes in Stagnant Electrolytes," *Electrochimica Acta* 50, no. 10 (2005): 2073–2079.
- 56. E. Padgett, G. Bender, A. Haug, et al., "Catalyst Layer Resistance and Utilization in PEM Electrolysis," *Journal of The Electrochemical Society* 170, no. 8 (2023): 084512.
- 57. F. Bao, E. Kemppainen, I. Dorbandt, et al., "Understanding the Hydrogen Evolution Reaction Kinetics of Electrodeposited Nickel-Molybdenum in Acidic, Near-Neutral, and Alkaline Conditions," *ChemElectroChem* 8, no. 1 (2021): 195–208.
- 58. A. T. Marshall and L. Vaisson-Béthune, "Avoid the Quasi-Equilibrium Assumption When Evaluating the Electrocatalytic Oxygen Evolution Reaction Mechanism by Tafel Slope Analysis," *Electrochemistry Communications* 61, 2015: 23–26.
- 59. L. J. J. Janssen, C. Sillen, E. Barendrecht, and S. J. D. Van Stralen, "Bubble Behaviour During Oxygen and Hydrogen Evolution at Transparent Electrodes in KOH Solution," *Electrochimica Acta* 29, no. 5 (1984): 633–642.
- 60. J. K. Lee, T. Schuler, G. Bender, et al., "Interfacial Engineering via Laser Ablation for High-Performing PEM Water Electrolysis," *Applied Energy* 336, (2023): 120853.
- 61. F. Rocha, R. Delmelle, C. Georgiadis, and J. Proost, "Effect of Pore Size and Electrolyte Flow Rate on the Bubble Removal Efficiency of 3D Pure Ni Foam Electrodes During Alkaline Water Electrolysis," *Journal of Environmental Chemical Engineering* 10, no. 3 (2022): 107648.

Supporting Information

Additional supporting information can be found online in the Supporting Information section.